Stripping back the Modern to reveal the Cenomanian-Turonian climate and temperature gradient underneath

Marie Laugié[1], Yannick Donnadieu[1], Jean-Baptiste Ladant[2], Mattias Green[3], Laurent Bopp[4,5] and François Raisson[6].

[1]Aix Marseille Univ, CNRS, IRD, INRA, Coll. France, CEREGE, Aix-en-Provence, France
[2]Department of Earth and Environmental Sciences, University of Michigan, Ann Arbor, MI, USA
[3]School of Ocean Sciences, Bangor University, Menai Bridge, UK
[4]Ecole Normale Supérieure (ENS Paris) - Département des Géosciences - France
[5]Laboratoire de Météorologie Dynamique (UMR 8539) (LMD) - Université Pierre et Marie Curie -
Paris 6, Institut national des sciences de l'Univers, École Polytechnique, École des Ponts ParisTech,
Centre National de la Recherche Scientifique : UMR8539, École Normale Supérieure - Paris - France
[6]Total EP – R&D Frontier Exploration - France

ABSTRACT

During past geological times, the Earth experienced several intervals of global warmth, but their driving factors remain equivocal. A careful appraisal of the main processes controlling past warm events is essential to inform future climates and ultimately provide decision makers with a clear understanding of the processes at play in a warmer world. In this context, intervals of greenhouse climates, such as the thermal maximum of the Cenomanian-Turonian (~94 Ma) during the Cretaceous period, are of particular interest. Here we use the IPSL-CM5A2 Earth System Model to unravel the forcing parameters of the Cenomanian-Turonian greenhouse climate. We perform six simulations with an incremental change in five major boundary conditions in order to isolate their respective role on climate change between the Cenomanian-Turonian and the preindustrial. Starting with a preindustrial simulation, we implement the following changes in boundary conditions: (1) the absence of polar ice sheets, (2) the increase in atmospheric pCO_2 to 1120 ppm, (3) the change of vegetation and soil parameters, (4) the 1% decrease in the Cenomanian-Turonian value of the solar constant and (5) the Cenomanian-Turonian paleogeography. Between the preindustrial simulation and the Cretaceous simulation, the model simulates a global warming of more than 11°C. Most of this warming is driven by the increase in atmospheric pCO_2 to 1120 ppm. Paleogeographic changes represent the second major contributor to global warming, whereas the reduction in the solar constant counteracts most of geographically-driven warming. We further demonstrate that the implementation of Cenomanian-Turonian boundary conditions flattens meridional temperature gradients compared to the preindustrial simulation. Interestingly, we show that paleogeography is the major driver of the flattening in the low- to mid-latitudes, whereas pCO_2 rise and polar ice sheet retreat dominate the high-latitude response.

1. INTRODUCTION

The Cretaceous period is of particular interest to understand drivers of past greenhouse climates because intervals of prolonged global warmth (O'Brien et al. 2017, Huber et al. 2018) and elevated atmospheric CO_2 levels (Wang et al., 2014), possibly similar to future levels, have been documented in the proxy record. The thermal maximum of the Cenomanian-Turonian (CT) interval (94 Ma) represents the acme of Cretaceous warmth, during which one of the most important carbon cycle perturbation of the Phanerozoic occurred: the oceanic anoxic event 2 (OAE2; Jenkyns, 2010; Huber et al., 2018). Valuable understanding of what controls large-scale climate processes can hence be drawn from investigations of the mechanisms responsible for the CT thermal maximum and carbon cycle perturbation.

Proxy-based reconstructions and model simulations of sea-surface temperatures (SST) for the CT reveal that during OAE2 the equatorial Atlantic was 4-6° warmer than today (Norris et al., 2002; Bice et al., 2006; Pucéat et al., 2007; Tabor et al., 2016), and possibly even warmer than that (6-9° - Forster et al., 2007). This short and abrupt episode of major climatic, oceanographic, and global carbon cycle perturbations occurred at the CT Boundary and was superimposed on a long period of global warmth (Jenkyns, 2010). The high latitudes were also much warmer than today (Herman and Spicer, 2010; Spicer and Herman, 2010), as was the abyssal ocean which experienced bottom temperatures reaching up to 20°C during the CT (Huber et al., 2002; Littler et al., 2011; Friedrich et al., 2012). Paleobotanical studies suggest that the atmosphere was also much warmer (Herman and Spicer, 1996), with high-latitude temperatures up to 17°C higher than today (Herman and Spicer, 2010) and possibly reaching annual means of 10-12°C in Antarctica (Huber et al., 1999).

The steepness of the equator-to-pole gradient is still a matter of debate, in particular because of inconsistencies between data and models as the latter usually predict steeper gradients than those reconstructed from proxy data (Barron, 1993; Huber et al., 1995; Heinemann et al., 2009; Tabor et al., 2016). Models and data generally agree, however, that Cretaceous sea-surface temperature (SST) gradients were reduced compared to today (Sellwood et al., 1994; Huber et al., 1995; Jenkyns et al., 2004; O'Brien et al., 2017; Robinson et al., 2019).

The main factor generally considered responsible for the Cretaceous global warm climate is the higher atmospheric CO_2 concentration (Barron et al., 1995; Crowley and Berner, 2001; Royer et al., 2007; Wang et al., 2014; Foster et al., 2017). This has been determined by proxy-data reconstructions of the Cretaceous pCO_2 using various techniques, including analysis of paleosols $\delta^{13}C$ (Sandler and Harlavan, 2006; Leier et al., 2009; Hong and

61   Lee, 2012), liverworts δ^{13}C (Fletcher et al., 2006) or phytane δ^{13}C (Damsté et al., 2008; Van Bentum et al., 2012)

62   and leaf stomata analysis (Barclay et al., 2010; Mays et al., 2015; Retallack and Conde, 2020). Modelling studies

63   have also focused on estimating Cretaceous atmospheric CO_2 levels (Barron et al., 1995; Poulsen et al., 2001,

64   2007; Berner, 2006; Bice et al., 2006; Monteiro et al., 2012) in an attempt to refine the large spread in values

65   inferred from proxy data (from less than 900 ppm to over 5000 ppm). The typical atmospheric pCO_2

66   concentration resulting from these studies for the CT averages around a long-term value of 1120 ppm (Barron et

67   al., 1995; Bice and Norris, 2003; Royer, 2013; Wang et al., 2014), e.g., four times the preindustrial value (280 ppm

68   = 1 P.A.L : "Preindustrial Atmospheric Level"). Atmospheric pCO_2 levels are, however, known to vary on shorter

69   timescales during the period, in particular during OAE2. It has indeed been suggested that this event may have

70   been caused by a large increase in atmospheric pCO_2 concentration, possibly reaching 2000 ppm or even higher,

71   because of volcanic activity in large igneous provinces (Kerr and Kerr, 1998; Turgeon and Creaser, 2008; Jenkyns,

72   2010). The proxy records suggest that the pCO_2 levels may have dropped down to 900 ppm after carbon

73   sequestration into organic-rich marine sediments (Van Bentum et al., 2012).

74   Paleogeography is also considered as a major driver of climate change through geological times (Crowley

75   et al., 1986; Gyllenhaal et al., 1991; Goddéris et al., 2014; Lunt et al., 2016). Several processes linked to

76   paleogeographic changes have been shown to impact Cretaceous climates. These processes include albedo and

77   evapotranspiration feedbacks from paleovegetation (Otto-bliesner and Upchurch, 1997), seasonality due to

78   continental break-up or presence of epicontinental seas (Fluteau et al., 2007), atmospheric feedbacks due to

79   water cycle modification (Donnadieu et al., 2006), Walker and Hadley cells changes after Gondwana break-up

80   (Ohba and Ueda, 2011), or oceanic circulation changes due to gateways opening (Poulsen et al., 2001, 2003).

81   Other potential controlling factors include the time-varying solar constant (Gough, 1981), whose impact on

82   Cretaceous climate evolution was quantified by Lunt et al. (2016), and changes in the distribution of vegetation,

83   which has been suggested to drive warming, especially in the high-latitudes with a temperature increase of up to

84   4°-10°C in polar regions (Otto-bliesner and Upchurch, 1997; Brady et al., 1998; Upchurch, 1998; Deconto et al.,

85   2000; Hunter et al., 2013).

86   Despite all these studies, there is no established consensus on the relative importance of each of the

87   controlling factors on the CT climate. In particular, the primary driver of the Cretaceous climate has been

88   suggested to be either pCO_2 or paleogeography. Early studies suggested a negligible role of paleogeography on

89   global climate compared to the high CO_2 concentration (Barron et al., 1995) whereas others suggested that CO_2

90 was not the primary control (Veizer et al., 2000) or that the impact of paleogeography on climate was as

91 important as a doubling of $p\text{CO}_2$ (Crowley et al., 1986). More recent modeling studies have also suggested that

92 paleogeographic changes could affect global climate (Poulsen et al., 2003; Donnadieu et al., 2006; Fluteau et al.,

93 2007) but their impact remain debated (Ladant and Donnadieu, 2016; Lunt et al., 2016; Tabor et al., 2016). For

94 example, the simulations of Lunt et al. (2016) support a key role of paleogeography at the regional rather than

95 global scale, and show that the global paleogeographic signal is cancelled by an opposite trend due to changes in

96 the solar constant. Tabor et al. (2016) also suggest important regional climatic impacts of paleogeography, but

97 argue that CO_2 is the main driver of the Late Cretaceous climate evolution. In contrast, Ladant and Donnadieu

98 (2016) find a large impact of paleogeography on the global mean Late Cretaceous temperatures; their signal is

99 roughly comparable to a doubling of atmospheric $p\text{CO}_2$. Finally, the role of paleovegetation is also uncertain as

00 some studies show a major role at high-latitude (Upchurch, 1998; Hunter et al., 2013), whereas a more recent

01 study instead suggests limited impact at high latitudes (<2°C) with a cooling effect at low latitudes under high

02 $p\text{CO}_2$ values (Zhou et al., 2012).

03   In this study, we investigate the forcing parameters of CT greenhouse climate by using a set of

04 simulations run with the IPSL-CM5A2 Earth System Model. We perform six simulations, using both preindustrial

05 and CT boundary conditions, where we incrementally modify the preindustrial boundary conditions to that of the

06 CT. The changes are as follows: (1) the removal of polar ice sheets, (2) an increase in $p\text{CO}_2$ to 1120 ppm, (3) the

07 change of vegetation and soil parameters, (4) a 1% reduction in the value of the solar constant, and (5) the

08 implementation of Cenomanian-Turonian paleogeography. We particularly focus on processes driving warming

09 or cooling of atmospheric surface temperatures after each change in boundary condition change to study the

10 relative importance of each parameter in the CT to preindustrial climate change. We also investigate how the SST

11 gradient responds to boundary condition changes to understand the evolution of its steepness between the CT

12 and the preindustrial.

14   2. MODEL DESCRIPTION & EXPERIMENTAL DESIGN

15 2.1 IPSL-CM5A2 MODEL

16   IPSL-CM5A2 is an updated version of the IPSL-CM5A-LR earth system model developed at IPSL (Institut

17 Pierre-Simon Laplace) within the CMIP5 framework (Dufresne et al., 2013). It is a fully-coupled Earth System

18 Model, which simulates the interactions between atmosphere, ocean, sea ice, and land surface. The model

19 includes the marine carbon and other key biogeochemical cycles (C, P, N, O, Fe and Si - See Aumont et al., 2015).

20 Its former version, IPSL-CM5A-LR, has a rich history of applications, including present-day and future climates

21 (Aumont and Bopp, 2006; Swingedouw et al., 2017) as well as preindustrial (Gastineau et al., 2013) and

22 paleoclimate studies (Kageyama et al., 2013; Contoux et al., 2015; Bopp et al., 2017; Tan et al., 2017; Sarr et al.,

23 2019). It was also part of IPCC AR5 and CMIP5 projects (Dufresne et al., 2013). IPSL-CM5A-LR has also been used

24 to explore links between marine productivity and climate (Bopp et al., 2013; Le Mézo et al., 2017; Ladant et al.,

25 2018), vegetation and climate (Contoux et al., 2013; Woillez et al., 2014), and topography and climate (Maffre et

26 al., 2018), but also the role of nutrients in the global carbon cycle (Tagliabue et al., 2010) or the variability of

27 oceanic circulation and upwelling (Ortega et al., 2015; Swingedouw et al., 2015). Building on recent technical

28 developments, IPSL-CM5A2 provides enhanced computing performances compared to IPSL-CM5A-LR, allowing

29 thousand year-long integrations required for deep-time paleoclimate applications or long-term future projections

30 (Sepulchre et al., 2019). It thus reasonably simulates modern-day and historical climates (despite some biases in

31 the tropics), whose complete description and evaluation can be found in Sepulchre et al., 2019.

32   IPSL-CM5A2 is composed of the LMDZ atmospheric model (Hourdin et al., 2013), the ORCHIDEE land

33 surface and vegetation model (including the continental hydrological cycle, vegetation, and carbon cycle; Krinner

34 et al., 2005) and the NEMO ocean model (Madec, 2012), including the LIM2 sea-ice model (Fichefet and

35 Maqueda, 1997) and the PISCES marine biogeochemistry model (Aumont et al., 2015). The OASIS coupler (Valcke

36 et al., 2006) ensures a good synchronization of the different components and the XIOS input/output parallel

37 library is used to read and write data. The LMDZ atmospheric component has a horizontal resolution of 96x95,

38 (equivalent to 3.75° in longitude and 1.875° in latitude) and 39 uneven vertical levels. ORCHIDEE shares the same

39 horizontal resolution whereas NEMO – the ocean component – has 31 uneven vertical levels (from 10 meters at

40 the surface to 500 meters at the bottom), and a horizontal resolution of approximately 2°, enhanced to up to 0.5°

41 in latitude in the tropics. NEMO uses the ORCA2.3 tripolar grid to overcome the North Pole singularity (Madec

42 and Imbard, 1996).

43

44 ## 2.2 EXPERIMENTAL DESIGN

45

46   Six simulations were performed for this study: one preindustrial control simulation, named piControl, and

47 five simulations for which the boundary conditions were changed one at a time to progressively reconstruct the

48   CT climate (see Table 1 for details). The scenarios are called 1X-NOICE (with no polar ice sheets), 4X-NOICE (no

49   polar ice sheets + pCO2 at 1120 ppm), 4X-NOICE-PFT-SOIL (previous changes + implementation of idealized Plant

50   Functional Types (PFTs) and mean parameters for soil), 4X-NOICE-PFT-SOIL-SOLAR (previous changes + reduction

51   of the solar constant) and 4X-CRETACEOUS (previous changes + CT paleogeography). The piControl simulation

52   has been run for 1800 years and the five others for 2000 years in order to reach near-surface equilibrium (see

53   Fig.1).

54

55   ## 2.2.1 BOUNDARY CONDITIONS

56

57   As most evidence suggests the absence of permanent polar ice sheets during the CT (MacLeod et al.,

58   2013; Ladant and Donnadieu, 2016; Huber et al., 2018), we remove polar ice sheets in our simulations (except in

59   piControl) and we adjust topography to account for isostatic rebound resulting from the loss of the land ice

60   covering Greenland and Antarctica (See Supplementary Figure 1). Ice sheets are replaced with brown bare soil

61   and the river routing stays unchanged.

62   In the 4X simulations (i.e., all except piControl and 1X-NOICE), pCO_2 is fixed to 1120 ppm (4 P.A.L), a value

63   reasonably close to the mean suggested by a recent compilation of CT pCO_2 reconstructions (Wang et al., 2014).

64   In the 4X-NOICE-PFT-SOIL simulation, the distribution of the 13 standard PFTs defined in ORCHIDEE is

65   uniformly reassigned along latitudinal bands, based on a rough comparison with the preindustrial distribution of

66   vegetation, in order to obtain a theoretical latitudinal distribution usable for any geological period. The list of

67   PFTs and associated latitudinal distribution and fractions are described in Supplementary Table 1. Mean soil

68   parameters, i.e., mean soil color and texture (rugosity), are calculated from preindustrial maps (Zobler, 1999;

69   Wilson and Henderson-sellers, 2003) and uniformly prescribed on all continents. The impact of these idealized

70   PFTs and mean parameters is discussed in the results.

71   The 4X-NOICE-PFT-SOIL-SOLAR simulation is initialized from the same conditions as 4X-NOICE-PFT-SOIL

72   except that the solar constant is reduced to its CT value (Gough, 1981). We use here the value of 1353.36 W/m^2

73   (98.9% of the modern solar luminosity, calculated for an age of 90 My).

74   The 4X-CRETACEOUS simulation, finally, incorporates the previous modifications plus the implementation

75   of the CT paleogeography. The land-sea configuration used here is that proposed by Sewall (2007), in which we

76   have implemented the bathymetry from Müller (2008) (see Fig. 2). These bathymetric changes are done to

77   represent deep oceanic topographic features, such as ridges, that are absent from the Sewall paleogeographic

78   configuration. In this simulation, the mean soil color and rugosity as well as the theoretical latitudinal PFTs

79   distribution are adapted to the new land-sea mask and the river routing is recalculated from the new topography.

80   We also modify the tidally driven mixing associated with dissipation o internal wave energy for the M2 and K1

81   tidal components from present day values (de Lavergne et al., 2019). The parameterization used for simulations

82   with the modern geography follows Simmons et al. (2004), with refinements in the modern Indonesian Through

83   Flow (ITF) region according to Koch-Larrouy et al. (2007). To create a Cenomanian-Turonian tidal dissipation

84   forcing, we calculate an M2 tidal dissipation field using the Oregon State University Tidal Inversion System

85   (OTIS, Egbert et al., 2004; Green and Huber, 2013). The M2 field is computed using our Cenomanian-Turonian

86   bathymetry and an ocean stratification taken from an unpublished equilibrated Cenomanian-Turonian simulation

87   realized with the IPSLCM5A2 with no M2 field. In the absence of any estimation for the CT, we prescribe the K1

88   tidal dissipation field to 0. In addition, the parameterization of Koch-Larrouy et al. (2007) is not used here

89   because the ITF does not exist in the Cretaceous.

90

91 ### 2.2.2 INITIAL CONDITIONS

92

93   The piControl and 1X-NOICE simulations are initialized with conditions from the Atmospheric Model

94   Intercomparison Project (AMIP) which were constrained by realistic sea surface temperature (SST) and sea ice

95   from 1979 to near present (Gates et al., 1999). In an attempt to reduce the integration time required to reach

96   near-equilibrium, the initial conditions of simulations with 4 PAL are taken from warm idealized conditions

97   (higher SST and no sea ice) adapted from those described in Lunt et al. (2017). The constant initial salinity field is

98   set to 34.7 PSU and ocean temperatures are initialized with a depth dependent distribution (see Sepulchre et al.,

99   GMD 2020, in review). In waters deeper than 1000 m, the temperature, T=10°C, whereas at depths shallower

00   than 1000 m it follows

01
$$T = 10 + \left(\frac{1000 - depth}{1000}\right) * 25\cos(latitude) \tag{1}$$

02

203 *Table 1 : Description of the simulations. The parameters in bold indicate the specific change for the corresponding simulation. Simulations are run for 2000 years, except piControl which is run*
204 *for 1000 years.*

Simulation	piControl	1X-NOICE	4X-NOICE	4X-NOICE-PFT-SOIL	4X-NOICE-PFT-SOIL-SOLAR	4X-CRETACEOUS
Polar Caps	Yes	**No**	No	No	No	No
CO_2 (ppm)	280	280	**1120**	1120	1120	1120
Vegetation	IPCC (1850)	IPCC (1850) + Bare soil instead of polar caps	IPCC (1850) + Bare soil instead of polar caps	**Theoretical latitudinal PFTs**	Theoretical latitudinal PFTs	Theoretical latitudinal PFTs
Soil Color/Texture	IPCC (1850)	IPCC (1850) + Brown soil instead of polar caps	IPCC (1850) + Brown soil instead of polar caps	**Uniform mean value**	Uniform mean value	Uniform mean value
Solar constant (W/m^2)	1365.6537	1365.6537	1365.6537	1365.6537	**1353.36**	1353.36
Geographic configuration	Modern	Modern	Modern	Modern	Modern	**Cretaceous 90 Ma (Sewall 2007 + Müller 2008)**

205

3. RESULTS

The simulated changes between the preindustrial (piControl) and the CT (4X-CRETACEOUS) simulations can be decomposed into five components based on our boundary condition changes: (1) Polar ice sheet removal (Δice), (2) pCO$_2$ (ΔCO$_2$), (3) PFT and Soil parameters (ΔPFT-SOIL), (4) Solar constant (Δsolar) and (5) Paleogeography (Δpaleo). Each contribution to the total climate change can be calculated by a linear factorization (Broccoli and Manabe, 1987; Von Deimling et al., 2006), which simply corresponds to the anomaly between two consecutive simulations. The choice of applying a linear factorization approach was made due to computing time and cost. We appreciate that another sequence of changes could lead to different intermediate states and could modulate the intensity of warming or cooling associated to each change. The computational costs would be too high for this study to explore this further here; it is an interesting problem that we leave for a future investigation. The results presented in the following are averages calculated over the last 100 simulated years.

3.1 GLOBAL CHANGES

The progressive change of parameters made to reconstruct the CT climate induces a general global warming (Table 2, Fig. 3). The annual global atmospheric temperature at 2 meters above the surface (T2M) rises from 13.25°C to 24.35 °C between the preindustrial and CT simulations. All changes in boundary conditions generates a warming signal on a global scale, with the exception of the decrease in solar constant which generates a cooling. Most of the warming is due to the fourfold increase in atmospheric pCO2, which alone increases the global mean temperature by 9°C. Paleogeographic changes also represent a major contributor to the warming, leading to an increase in T2M of 2.6°C. In contrast, the decrease in solar constant leads to a cooling of 1.8°C at the global scale. Finally, changes in the soil parameters and PFTs, as well as the retreat of polar caps, have smaller impacts, leading to increases in global mean T2M of 0.8°C and 0.5°C respectively.

Temperature changes exhibit different geographic patterns (Fig. 4) depending on which parameter is changed. These patterns range from global and uniform cooling (Δsolar – Fig 4e) to a global, polar-amplified, warming (ΔpCO$_2$ – Fig 4c), as well as heterogeneous regional responses (Δice or Δpaleo – Fig 4b and 4f). In the next section, we describe the main patterns of change and the main feedbacks arising.

	piControl	1X-NOICE	4X-NOICE	4X-NOICE-PFT-SOIL	4X-NOICE-PFT-SOIL-SOLAR	4X-CRETACEOUS
T2M (°C)	13.25	13.75	22.75	23.55	21.75	24.35
Planetary Albedo (%)	33.1	32.6	28.8	28.3	28.7	27.1
Surface Albedo (%)	20.1	19	16.6	15.5	15.3	14.9
Emissivity (%)	62	61.7	57.5	57.1	57.8	57

Table 2: Simulations results (Global annual mean over last 100 years of simulation.

3.2 The major contributor to global warming - ΔCO_2

As mentioned above, the fourfold increase in $p CO_2$ leads to a global warming of 9°C (Table 3, Fig. 3) between the 1X-NOICE and the 4X-NOICE simulations. The whole Earth warms, with an amplification located over the Arctic and Austral oceans and a warming generally larger over continents than over oceans (Fig 4c). The warming is due to a general decrease of planetary albedo and of the atmosphere's emissivity (see Supplementary Figure 2). The decrease in the atmosphere's emissivity is directly driven by the increase in CO_2, and thus greenhouse trapping in the atmosphere. It is also amplified by an increase in high-altitude cloudiness (defined as cloudiness at atmospheric pressure < 440 hPa) over the Antarctic continent (Fig 5a, b). The decrease in planetary albedo is due to two major processes. First, a decrease of sea ice and snow cover (especially over Northern Hemisphere continents and along the coasts of Antarctica), leading to surface albedo decrease, explains the warming amplification over polar oceans and continents. Second, a decrease in low-altitude cloudiness (defined as cloudiness at atmospheric pressure > 680 hPa) at all latitudes except over the Arctic (Fig 5a, b) leads to an increase in absorbed solar radiation.

The contrast in the atmospheric response over continents and oceans is due to the impact of the evapo-transpiration feedback. Oceanic warming drives an increase in evaporation, which acts as a negative feedback and moderates the warming by consuming more latent heat at the ocean surface. In contrast, high temperatures resulting from continental warming tend to inhibit vegetation development, which acts as positive feedback and enhances the warming due to reduced transpiration and reduced latent heat consumption.

3.3 Boundary conditions with the smallest global impact – Δice, ΔPFT-SOIL, Δsolar

The removal of polar ice sheets in the 1X-NOICE simulation leads to a weak global warming of 0.5°C but a strong regional warming observed over areas previously covered by the Antarctic and Greenland ice sheets (Fig 4a, b). This signal is due to the combination of a decrease in elevation (i.e., lapse rate feedback – Supplementary Figure S3) and in surface albedo, which is directly linked to the

265   shift from a reflective ice surface to a darker bare soil surface. Unexpected cooling is also simulated in

266   specific areas, such as the margins of the Arctic Ocean and the southwestern Pacific. These contrasted

267   climatic responses to the impact of ice sheets on sea surface temperatures are consistent with

268   previous modeling studies (Goldner et al., 2014; Knorr and Lohmann, 2014; Kennedy et al., 2015).

269   Their origin is still unclear but changes in winds in the Southern Ocean, due to topographic changes

270   after polar ice sheet removal, may locally impact oceanic currents, deep-water formation, and thus

271   oceanic heat transport and temperature distribution. In the Northern Hemisphere, the observed

272   cooling over Eurasia could be linked to stationary wave feedbacks following changes in topography

273   after Greenland ice sheet removal (Supplementary Figure S4; see also Maffre et al., 2018).

274   The change in soil parameters and the implementation of theoretical zonal PFTs in the 4X-

275   NOICE-PFT-SOIL simulation drive a warming of 0.8 °C. This warming is essentially located above arid

276   areas, such as the Sahara, Australia, or Middle East, and polar latitudes (Antarctica/Greenland) (Fig

277   4d), and is mostly caused by the implementation of a mean uniform soil color, which drives a surface

278   albedo decrease over deserts that normally have a lighter color. The warming at high-latitudes is

279   linked to vegetation change: bare soil that characterizes continental regions previously covered with

280   ice is replaced by boreal vegetation with a lower surface albedo. The presence of vegetation at such

281   high-latitudes is consistent with high-latitude paleobotanical data and temperature records during the

282   Cretaceous (Otto-bliesner and Upchurch, 1997; Herman and Spicer, 2010; Spicer and Herman, 2010).

283   Finally, the change in solar constant from 1365 W/m^2 to 1353 W/m^2 (Gough 1981) directly

284   drives a cooling of 1.8 °C evenly distributed over the planet (Fig 4e).

285

286   3.4 The most complex response - Δpaleogeography

287   The paleogeographic change drives a global warming of 2.6 °C. This is seen year-round in the

288   Southern Hemisphere, while the Northern Hemisphere experiences a warming during winter and

289   cooling during summer compared to the 4X-NI-PFT-SOIL-SOLAR simulation (Fig 6). These temperature

290   changes are linked to a general decrease in planetary albedo and/or emissivity, although the Northern

291   Hemisphere sometimes exhibits increased albedo, due to the increase in low-altitude cloudiness. This

292   increase in albedo is compensated by a strong atmosphere emissivity decrease during winter but not

293   during summer, which leads to the seasonal pattern of cooling and warming (Supplementary Figure

294   S5).

295   The albedo and emissivity changes are linked to atmospheric and oceanic circulation

296   modifications driven by four major features of the CT paleogeography (Fig 2):

297   (1) Equatorial oceanic gateway opening (Central American Seaway/Neotethys)

298   (2) Polar gateway closure (Drake/Tasman)

299   (3) Increase in oceanic area in the North Hemisphere (Fig 2)

300   (4) Decrease in oceanic area in the South Hemisphere (Fig 2)

301

302   In the CT simulation, we observe an intensification of the meridional surface circulation and

303   extension towards higher latitudes compared to the simulation with the modern geography (Fig8a-b),

304   as well as an intensification of subtropical gyres, especially in the Pacific (Supplementary Figure S6),

305   which are responsible for an increase in poleward oceanic heat transport (OHT – Fig 8c). Such

306   modifications can be linked to the opening of equatorial gateways that creates a zonal connection

307   between the Pacific, Atlantic and Neotethys oceans (Enderton and Marshall, 2008; Hotinski and

308   Toggweiler, 2003) and that leads to the formation of a strong circumglobal equatorial current (Fig 7b) .

309   This connection permits the existence of stronger easterly winds that enhance equatorial upwelling

310   and drive increased export of water and heat from low latitudes to polar regions. In the Southern

311   Hemisphere, the Drake Passage is only open to shallow flow, and the Tasman gateway has not yet

312   formed. The closure of these zonal connections leads to the disappearance of the modern Antarctic

313   Circumpolar Current (ACC) during the Cretaceous (Fig 7c-d). Notwithstanding, the observed increase

314   in southward OHT between 40° and 60°S (Fig 8c) is explained by the absence of significant zonal

315   connections in the Southern Ocean, which allows for the buildup of polar gyres in the CT simulation

316   (Supplementary Figure S6).

317   The increase in OHT is associated with a meridional expansion of high sea-surface

318   temperatures leading to an intensification of evaporation between the tropics and a poleward shift of

319   the ascending branches of the Hadley cells. The combination of these two processes results in a

320   greater injection of moisture into the atmosphere between the tropics (Supplementary Figure S7).

321   Consequently, the high-altitude cloudiness increases and spreads towards the tropics, leading to an

322   enhanced greenhouse effect. This process is the main driver of the intertropical warming (Herweijer et

323   al., 2005; Levine and Schneider, 2010; Rose and Ferreira, 2013).

324   The atmosphere's response to the paleogeographic changes in the mid- and high-latitudes is

325   different in the Southern and Northern Hemispheres because the ocean to land ratio varies between

326   the CT configuration and the modern. In the Southern Hemisphere, the reduced ocean surface area in

327   the CT simulation (Fig 2) limits evaporation and moisture injection into the atmosphere, which in turn

328   leads to a decrease in relative humidity and low-altitude cloudiness (Supplementary Fig S8) and

329   associated year-round warming due to reduced planetary albedo. In the Northern Hemisphere,

330   oceanic surface area increases (Fig 2) and results in a strong increase in evaporation and moisture

331   injection into the atmosphere. Low-altitude cloudiness and planetary albedo increase and lead to

332   summer cooling, as discussed above (Fig 6). During winter an increase in high-altitude cloudiness leads

333   to an enhanced greenhouse effect and counteracts the larger albedo. This high-altitude cloudiness

334 increase is consistent with the simulated increase in extratropical OHT (Fig. 8). Mid-latitude

335 convection and moist air injection into the upper troposphere is consequently enhanced and

336 efficiently transported poleward (Rose and Ferreira, 2013; Ladant and Donnadieu, 2016). In addition,

337 increased continental fragmentation in the CT paleogeography relative to the preindustrial decreases

338 the effect of continentality (Donnadieu et al. 2006) because thermal inertia is greater in the ocean

339 than over continents.

340

341 3.5 Temperature Gradients

342 3.5.1 Ocean

343   The mean annual global SST increases as much as 9.8°C (from 17.9°C to 27.7 °C) across the

344 simulations. The SST warming is slightly weaker than that of the mean annual global atmospheric

345 temperature at 2m discussed above, and most likely occurs because of evaporation processes due to

346 the weaker atmospheric warming simulated above oceans compared to that simulated above

347 continents. Unsurprisingly, as for the atmospheric temperatures, pCO_2 is the major controlling

348 parameter of the ocean warming (7°C), followed by paleogeography (4.5°C) and changes in the solar

349 constant (2.3°C), although the latter induces a cooling rather than a warming. PFT and soil parameter

350 changes and the removal of polar ice sheets have a minor impact at the global SST (0.6 °C and 0°C

351 respectively). It is interesting to note the increased contribution of paleogeography to the simulated

352 SST warming compared to its contribution to the simulated atmospheric warming, which is probably

353 driven by the major changes simulated in surface ocean circulation (Fig. 7).

354   Mean annual SST in the preindustrial simulation reach ~ 26°C in the tropics (calculated as the

355 zonal average between 30°S and 30°N) and ~ -1.5°C at the poles (beyond 70° N - Fig 9a). In this work,

356 we define the meridional temperature gradients as the linear temperature change per 1° of latitude

357 between 30° and 80°. The gradients in the piControl experiment then amount to 0.45°C/°latitude and

358 0.44°C/°latitude for the Northern and Southern Hemispheres, respectively. In the CT simulation, the

359 mean annual SST reach ~ 33.3°C in the tropics, and ~5°C and 10°C in the Arctic and Southern Ocean

360 respectively, and the simulated CT meridional gradients are 0.45°C/°latitude and 0.39°C/°latitude for

361 the Northern and Southern Hemispheres, respectively.

362   The progressive flattening of the SST gradient can be visualized by superimposing the zonal

363 mean temperatures of the different simulations and by adjusting them at the Equator (Fig 9b). Two

364 major observations can be drawn from these results. First, paleogeography has a strong impact on the

365 low-latitudes (< 30° of latitude) SST gradient because it widens the latitudinal band of relatively

366 homogeneous warm tropical SST as a result of the opening of equatorial gateways. Second, poleward

367 of 40° in latitude, the paleogeography and the increase in atmospheric pCO_2 both contribute to the

368   flattening of the SST gradient with a larger influence from paleogeography than from atmospheric

369   pCO$_2$.

370

371   3.5.2 Atmosphere

372   In the preindustrial simulation, mean tropical atmospheric temperatures reach ~ 23.6°C

373   whereas polar temperatures (calculated as the average between 80° and 90° of latitude) in the

374   Northern and Southern Hemispheres reach around -16.8°C and -37°C respectively. The northern

375   meridional temperature gradient is 0.69°C/°latitude while the southern latitudinal temperature

376   gradient is 1.07°C/°latitude (Fig 9c). This significant difference is explained by the very negative mean

377   annual temperatures over Antarctica linked to the presence of the ice sheet.

378   In the CT simulation, mean tropical atmospheric temperatures reach ~ 32.3°C whereas polar

379   temperatures reach ~ 3.4°C in the Northern Hemisphere and ~ - 0.5°C in the Southern Hemisphere,

380   thereby yielding latitudinal temperature gradients of 0.49°C/°latitude and 0.54°C/°latitude,

381   respectively. The gradients are reduced compared to the preindustrial because the absence of year-

382   round sea and land ice at the poles drives leads to far higher polar temperatures.

383   As for the SST gradients, we plot atmospheric meridional gradients by adjusting temperature

384   values so that temperatures at the Equator are equal for each simulation (Fig 9d). This normalization

385   reveals that the mechanisms responsible for the flattening of the gradients are different for each

386   hemisphere. In the Southern Hemisphere high-latitudes (> 60° of latitude), three parameters

387   contribute to reducing the equator-to-pole temperature gradient in the following order of

388   importance: removal of polar ice sheets, paleogeography and increase in atmospheric pCO$_2$. In

389   contrast, the reduction in the gradient steepness in the Northern Hemisphere high-latitudes is

390   exclusively explained by the increase in atmospheric pCO$_2$. In the low- and mid-latitudes, this

391   temperature gradient reduction is essentially explained by paleogeography in the Southern

392   Hemisphere and by a similar contribution of paleogeographic changes and increase in atmospheric

393   pCO$_2$ in the Northern Hemisphere.

394   4. DISCUSSION
395
396   4.1 CENOMANIAN-TURONIAN MODEL/DATA COMPARISON

397   The results predicted by our CT simulation can be compared to reconstructions of

398   atmospheric and oceanic paleotemperatures inferred from proxy data (Fig 10a, b). Our SST data

399   compilation is modified version of Tabor et al (2016), with additional data from more recent studies

400   (see our Supplementary data). We also compiled atmospheric temperature data obtained from

401 paleobotanical and paleosoil studies (see Supplementary data for the complete database and

402 references).

403   The Cretaceous equatorial and tropical SST have long been believed to be similar or even

404 lower than those of today (Sellwood et al., 1994; Crowley and Zachos, 1999; Huber et al., 2002), thus

405 feeding the problem of "tropical overheating" systematically observed in General Circulation Model

406 simulations (Barron et al., 1995; Bush et al., 1997; Poulsen et al., 1998). This incongruence was based

407 on the relatively low tropical temperatures reconstructed from foraminiferal calcite (25-30°C, Fig. 9a),

408 but subsequent work suggested that these were underestimated because of diagenetic alteration

409 (Pearson et al., 2001; Pucéat et al., 2007). Latest data compilations including temperature

410 reconstructions from other proxies, such as TEX86, have provided support for high tropical SST in the

411 Cenomanian-Turonian (Tabor et al., 2016; O'Brien et al., 2017) and our tropical SST are mostly

412 consistent with existing paleotemperature reconstructions (Fig. 10a). In the mid-latitudes (30-60°),

413 proxy records infer a wide range of possible SST, ranging from 10°C to more than 30°C. Simulated

414 temperatures in our CT simulation reasonably agree with these reconstructions if seasonal variability,

415 represented by local monthly maximum and minimum temperatures (grey shaded areas, Fig 10a), is

416 considered. This congruence would imply that a seasonal bias may exist in temperatures

417 reconstructed from proxies, which is suggested in previous studies (Sluijs et al., 2006; Hollis et al.,

418 2012; Huber, 2012; Steinig et al., 2020) but still debated (Tierney, 2012). There are unfortunately only

419 a few high-latitudes SST data points available, which render the model-data comparison difficult. In

420 the Northern Hemisphere, the presence of crocodilian fossils (Vandermark et al., 2007) in the

421 northern Labrador Sea (~70° of latitude) imply mean annual temperature of at least 14°C and

422 temperature of the coldest month of at least 5°C. In comparison, simulated temperatures at the same

423 latitude in the adjacent Western Interior Sea are very similar (13.5 °C for the annual mean and 7.9 °C

424 for the coldest month). In the Southern Hemisphere, mean annual SST calculated from foraminiferal

425 calcite at DSDP sites 511 and 258 are between 25° and 28°C (Huber et al., 2018). Simulated annual SST

426 reach a monthly maximum of 28°C around the location of site DSDP 258. We speculate that a seasonal

427 bias in the foraminiferal record may represent a possible cause for this difference; alternatively, local

428 deviations of the regional seawater $\delta^{18}O$ from the globally assumed -1‰ value may also reduce the

429 model-data discrepancy (Zhou et al., 2008; Zhu et al., 2020).

430   To our knowledge, atmospheric temperature reconstructions from tropical latitudes are not

431 available. In the mid-latitudes (30-60°), simulated atmospheric temperatures in the Southern

432 Hemisphere reveal reasonable agreement with data whereas Northern Hemisphere mean zonal

433 temperatures in our model are slightly warmer than that inferred from proxies (Fig 10b). At high-

434 latitudes, the same trend is observed for atmospheric temperatures as it is for SST with data indicating

435 higher temperatures than the model in both the Southern and Northern Hemispheres. This inter-

436   hemispheric symmetry in model-data discrepancy could indicate a systematic cool bias of the

437   simulated temperatures.

438   4.2 RECONSTRUCTED LATITUDINAL TEMPERATURE GRADIENTS

439   The simulated northern hemisphere latitudinal SST gradient of (~0.45°C/°latitude) is in good

440   agreement with those reconstructed from paleoceanographic data in the Northern Hemisphere

441   (~0.42°C/°latitude) whereas it is much larger in the Southern Hemisphere (~0.39°C/°latitude vs

442   ~0.3°C/°latitude) (Fig 11). This overestimate of the latitudinal gradient holds for the atmosphere as

443   well, as gradients inferred from data are much lower (North=0.2°C/°latitude and

444   South=0.18°C/°latitude) than simulated gradients (North=0.49°C/°latitude and

445   South=0.55°C/°latitude), although the paucity of Cenomanian-Turonian continental temperatures

446   proxy data is likely to significantly bias this comparison.

447   In the following, we compare our simulated gradients to those obtained in previous deep time

448   modelling studies using recent earth system models. Because Earth system models studies focusing on

449   the Cenomanian-Turonian are limited in numbers, we include simulations of the Early Eocene (~ 55

450   Ma), which is another interval of global climatic warmth (Lunt et al., 2012a, 2017) (Fig. 11). The

451   simulated SST latitudinal gradients range from 0.32°C/°latitude to 0.55°C/°latitude (Lunt et al., 2012;

452   Tabor et al., 2016; Zhu et al., 2019; Fig. 11) and the atmospheric latitudinal gradients from

453   0.33°C/°latitude to 0.78°C/°latitude (Huber and Caballero, 2011; Lunt et al., 2012; Niezgodzki et al.,

454   2017; Upchurch et al., 2015; Zhu et al., 2019; Fig. 11). For a single model and a single set of boundary

455   conditions (Cretaceous or Eocene), the lowest latitudinal gradient is obtained for the highest pCO$_2$

456   value. However, when comparing different studies with the same model (Cretaceous vs Eocene using

457   the ECHAM5 model; Lunt et al., 2012a; Niezgodzki et al., 2017) it is not the case: the South

458   Hemisphere atmospheric gradient obtained for the Eocene with the ECHAM5 model is always lower

459   than those obtained for the Cretaceous with the same model, regardless of the pCO$_2$ value (Fig. 11

460   and Supplementary Data). These results show the major role of boundary conditions (in particular

461   paleogeography) in defining the latitudinal temperature gradient. IPSL-CM5A2 predicts SST and

462   atmosphere gradients that are well within the range of other models of comparable resolution and

463   complexity. Models almost systematically simulate larger gradients than those obtained from data

464   (Fig. 11, see also Huber, 2012). The reasons behind this incongruence are debated (Huber, 2012) but

465   highlight the need for more data and for challenging the behavior of complex earth system models, in

466   particular in the high latitudes. Studies have demonstrated that models are able to simulate lower

467   latitudinal temperature gradients under specific conditions such as anomalously high CO$_2$

468   concentrations (Huber and Caballero, 2011), modified cloud properties and radiative

469   parameterizations (Upchurch et al., 2015; Zhu et al., 2019) or lower paleo elevations and/or more

470   extensive wetlands (Hay et al., 2019). Finally, from a proxy perspective, it has been suggested that a

471   sampling bias could exist, with a better record of temperatures during the warm season at high

472   latitudes and during the cold season in low latitudes (Huber, 2012). Such possible biases would help

473   reduce the model-data discrepancy, in particular for atmospheric temperatures (Fig 10b), as high-

474   latitude reconstructed temperatures are more consistent with simulated summer temperatures

475   whereas the consistency is better with simulated winter temperatures in the mid- to low-latitudes, but

476   further work is required to unambiguously demonstrate the existence of these biases.

477

478   4.3 PRIMARY CLIMATE CONTROLS
479

480   The earliest estimates of climate sensitivity (or the temperature change under a doubling of

481   the atmospheric pCO$_2$) predicted a 1.5 to 4.5°C temperature increase, with the most likely scenario

482   providing an increase of 2.5°C (Charney et al., 1979; Barron et al., 1995; Sellers et al., 1996; IPCC,

483   2014). Our modelling study predicts an atmospheric warming of 11.1°C for the CT. The signal is

484   notably due to a 9°C warming in response to the fourfold increase in pCO$_2$, which converts to an

485   increase of 4.5°C for a doubling of pCO$_2$ (assuming a linear response). This climate sensitivity agrees

486   with the higher end of the range of previous estimates (Charney et al., 1979; Barron et al., 1995;

487   Sellers et al., 1996; IPCC, 2014). However, our simulated climate sensitivity could be slightly lower as

488   the simulations are not completely equilibrated (Fig. 1). The latest generation of Earth system models

489   used in deep-time paleoclimate also show an increasingly higher climate sensitivity to increased CO$_2$

490   (Hutchinson et al., 2018; Golaz et al., 2019; Zhu et al., 2019), suggesting that the sensitivity could have

491   been underestimated in earlier studies. For example, the recent study of Zhu (2019), using an up-to-

492   date parameterization of cloud microphysics in the CESM1.2 model, proposes an Eocene Climate

493   Sensitivity of 6.6°C for a doubling of CO$_2$ from 3 to 6 PAL.

494   We have shown that pCO$_2$ is the main controlling factor for atmospheric global warming

495   whereas the effects of the paleogeography (warming) and reduced solar constant (cooling) nearly

496   cancel each other out at the global scale (see also Lunt et al., 2016). These results agree with previous

497   studies suggesting that pCO$_2$ is the main factor controlling climate (Barron et al., 1995; Crowley and

498   Berner, 2001; Royer et al., 2007; Foster et al., 2017). However, we also demonstrate that

499   paleogeography plays a major role in the latitudinal distribution of temperatures and impacts oceanic

500   temperatures (with a similar magnitude than a doubling of pCO$_2$), thus confirming that it is also a

501   critical driver of the Earth's climate (Poulsen et al., 2003; Donnadieu et al., 2006; Fluteau et al., 2007;

502   Lunt et al., 2016). The large climatic influence of the continental configuration has not been reported

503   for paleogeographic configurations closer to each other, e.g., the Maastrichtian and Cenomanian

504   (Tabor et al., 2016). The main features influencing climate in our study (i.e. the configuration of

505   equatorial and polar zonal connections and the land/sea distribution) are indeed not fundamentally

506   different in the two geological periods investigated by Tabor et al. (2016). Paleogeography is thus a

507   first-order control on climate over long timescales.

508   Early work has suggested that high latitude warming can be amplified in deep time simulations

509   by rising CO_2 via cloud and vegetation feedbacks (Otto-bliesner and Upchurch, 1997; Deconto et al.,

510   2000) or by increasing ocean heat transport (Barron et al., 1995; Schmidt and Mysak, 1996; Brady et

511   al., 1998), in particular when changing the paleogeography (Hotinski and Toggweiler, 2003). Our study

512   confirms that the paleogeography is a primary control on the steepness of the oceanic meridional

513   temperature gradient. Furthermore, paleogeography is the only process, among those investigated,

514   that controls both the atmosphere and ocean temperature gradients in the tropics and it has a greater

515   impact than atmospheric CO_2 on the reduction of the atmospheric temperature gradient at high

516   latitudes in the Southern Hemisphere between the CT and the preindustrial. The increase in pCO_2

517   appears as the second most important parameter controlling the SST gradient at high latitudes and is

518   the main control of the reduced atmospheric gradient in the Northern Hemisphere due to low cloud

519   albedo feedback. The effect of paleovegetation on the reduced temperature gradient is marginal at

520   high latitudes in our simulations, in contrast to the significant warming reported in early studies (Otto-

521   bliesner and Upchurch, 1997; Upchurch, 1998; Deconto et al., 2000) but in agreement with more

522   recent model simulations suggesting a limited influence of vegetation in the Cretaceous high-latitudes

523   warmth (Zhou et al., 2012). However, our modeling setup prescribes boreal vegetation at latitudes

524   higher than 50° whereas evidence exist to support the development of evergreen forests poleward of

525   60° of latitude (Sewall et al., 2007; Hay et al., 2019) and of temperate forests up to 60° of latitude

526   (Otto-bliesner and Upchurch, 1997). The presence of such vegetation types could change the albedo

527   of continental regions but also heat and water vapor transfer by altered evapo-transpiration

528   processes, thus leading to warming amplification at high-latitudes and reduced temperature gradients

529   (Otto-bliesner and Upchurch, 1997; Hay et al., 2019). Based on these studies and on our results, we

530   cannot exclude that different types of high-latitude could promote a greater impact of

531   paleovegetation in reducing the temperature gradient.

532

533   ## 5. CONCLUSIONS

534   To quantify the impact of major climate forcings on the Cenomanian-Turonian climate, we

535   perform a series of 6 simulations using the IPSL-CM5A2 earth system model in which we incrementally

536   implement changes in boundary conditions on a preindustrial simulation to obtain ultimately a

537   simulation of the Cenomanian-Turonian stage of the Cretaceous. This study confirms the primary

538   control exerted by atmospheric pCO_2 on atmospheric and sea-surface temperatures, followed by

539   paleogeography. In contrast, the flattening of meridional SST gradients between the preindustrial and

540   the CT is mainly due to paleogeographic changes and to a lesser extent to the increase in $p\mathrm{CO}_2$. The

541   atmospheric gradient response is more complex because the flattening is controlled by several factors

542   including paleogeography, pCO2 and polar ice sheet retreat. While predicted oceanic and atmospheric

543   temperatures show reasonable agreement with data in the low and mid latitudes, predicted

544   temperatures in the high latitudes are colder than paleotemperatures reconstructed from proxies,

545   which leads to steeper equator-to-pole gradients in the model than those inferred from proxies.

546   However, this mismatch, often observed in data-model comparison studies, has been reduced in the

547   last decades and could be further resolved by considering possible sampling/seasonal biases in the

548   proxies and by continuously improving model physics and parameterizations.

549

DATA AVAILABILITY

551   Code availability:

552   LMDZ, XIOS, NEMO and ORCHIDEE are released under the terms of the CeCILL license. OASIS-MCT is

553   released under the terms of the Lesser GNU General Public License (LGPL). IPSL-CM5A2 code is

554   publicly available through svn, with the following command lines: svn co

555   http://forge.ipsl.jussieu.fr/igcmg/svn/modipsl/branches/publications/IPSLCM5A2.1_11192019

556   modipsl

557   cd modipsl/util;./model IPSLCM5A2.1

558   The mod.def file provides information regarding the different revisions used, namely:

559   – NEMOGCM branch nemo_v3_6_STABLE revision 6665

560   – XIOS2 branchs/xios-2.5 revision 1763

561   – IOIPSL/src svn tags/v2_2_2

562   – LMDZ5 branches/IPSLCM5A2.1 rev 3591

563   – branches/publications/ORCHIDEE_IPSLCM5A2.1.r5307 rev 6336

564   – OASIS3-MCT 2.0_branch (rev 4775 IPSL server)

565   The login/password combination requested at first use to download the ORCHIDEE component is

566   anonymous/anonymous. We recommend to refer to the project website:

567   http://forge.ipsl.jussieu.fr/igcmg_doc/wiki/Doc/Config/IPSLCM5A2 for a proper installation and

568   compilation of the environment.

569

570   Data availability: Data that support the results of this study, as well as boundary condition files are

571   available on request to the authors.

AUTHOR CONTRIBUTION

572   M.L performed and analyzed the numerical simulations, in close cooperation with Y.D and J.B.L, and

573

574   led the writing. M.G run the OTIS model to provide the Cenonamian-Turonian tidal dissipation. All

575   authors discussed the results and analyses presented in the final version of the manuscript.

COMPETING INTERESTS

576

577   The authors declare that they do not have competing interests.

AKNOWLEDGMENTS

578

579   We express our thanks to Total E&P for funding the project and granting permission to publish. We

580   thank the CEA/CCRT for providing access to the HPC resources of TGCC under the allocation 2018-

581   GEN2212 made by GENCI. J.A.M.G receives funding from the Natural Environmental Research Council

582   (grant NE/S009566/1, MATCH). We acknowledge use of the Ferret (ferret.pmel.noaa.gov/Ferret/)

583   program for analysis and graphics in this paper.

FIGURES

584

585

Figure 1: Time series for mean annual oceanic temperatures. (a) Sea-surface temperature and (b) deep-ocean (2500 m) temperature. The piControl and 1X-NOICE simulations are perfectly equilibrated. The 4X simulations still have a small linear drift, around 0.1°C/century or less : 0.07, 0.08, 0.05 and 0.01°C/century during the last 500 years for SST of 4X-NOICE, 4X-NOICE-PFT-SOIL, 4X-NOICE-PFT-SOIL-SOLAR and 4X-CRETACEOUS respectively; 0.11, 0.08, 0.07 and 0.06°C/century during the last 500 years, for deep-ocean of 4X-NOICE, 4X-NOICE-PFT-SOIL, 4X-NOICE-PFT-SOIL-SOLAR and 4X-CRETACEOUS respectively.
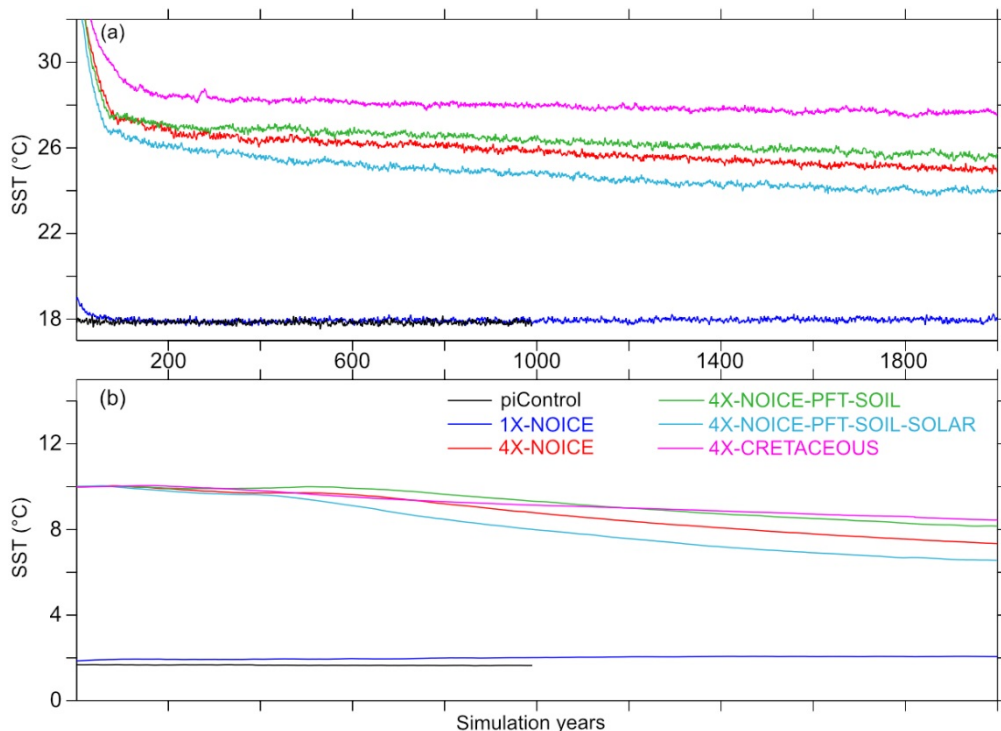
Figure 2: Modern and Cenomanian-Turonian geographic configurations used for the piControl and 4X-CRETACEOUS simulations respectively, and meridional oceanic area anomaly between Cretaceous paleogeography and Modern. geography.
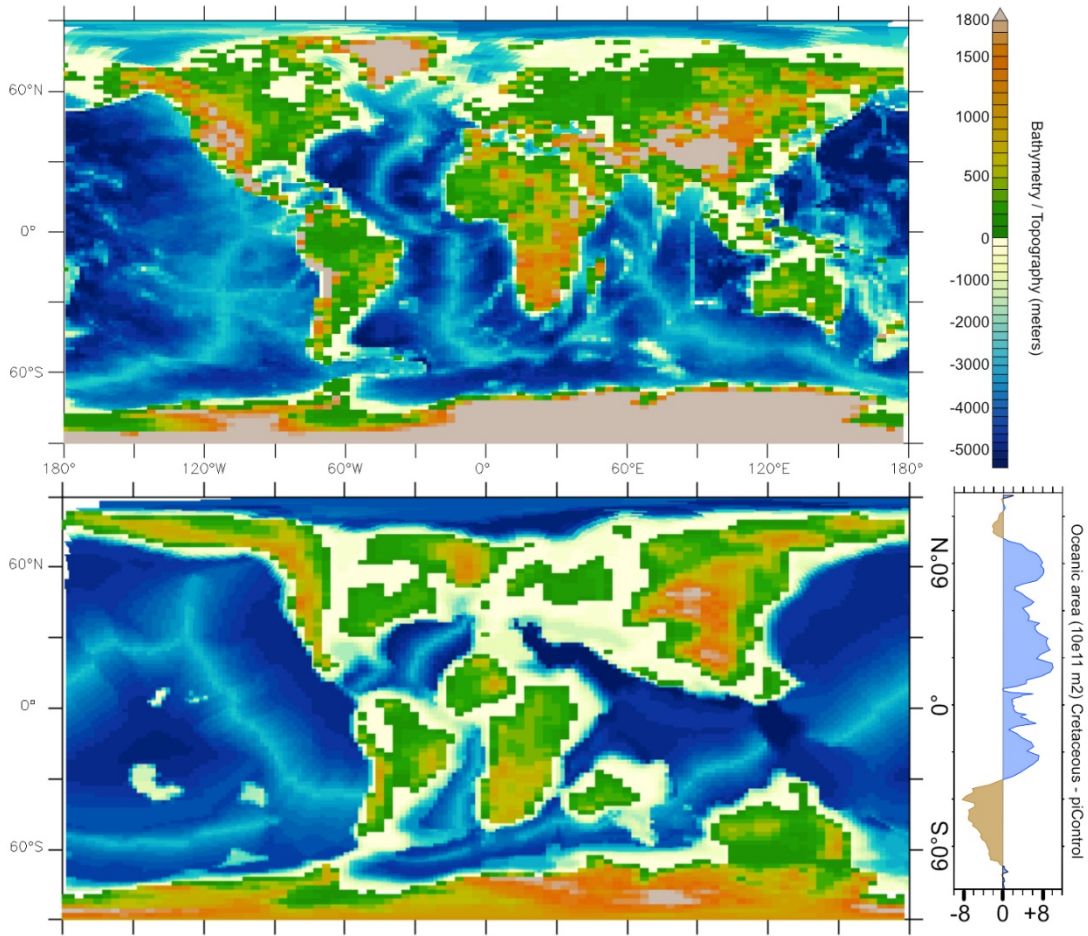
Figure 3: Evolution of Albedo (surface and planetary) and emissivity, in percentages and of T2M (°C) from piControl to 4X-CRETACEOUS simulations. The major change is always recorded with the change of pCO_2 between 1X-NOICE and 4X-NOICE simulations.
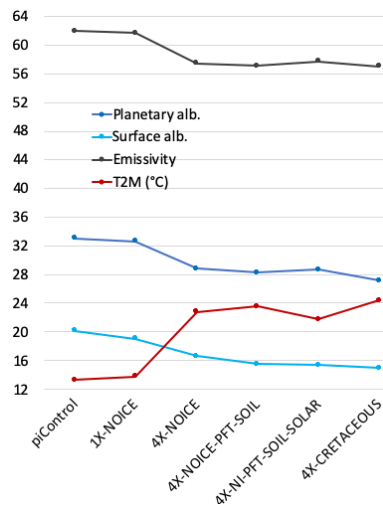
Figure 4: T2M (°C) for (a) piControl initial simulation and (g) Cretaceous final simulation, and anomalies (°C) for intermediate simulations: (b) 1X-NOICE-piControl, (c) 4X-NOICE-1X-NOICE, (d) 4X-NOICE-PFT-SOIL – 4X-NOICE, (e) 4X-NOICE-PFT-SOIL-SOLAR – 4X-NOICE-PFT-SOIL, (f) 4X-CRETACEOUS - 4X-NOICE-PFT-SOIL. White color (not represented in the colourbar) correspond to areas where the anomaly is not statistically significative according to the student test.
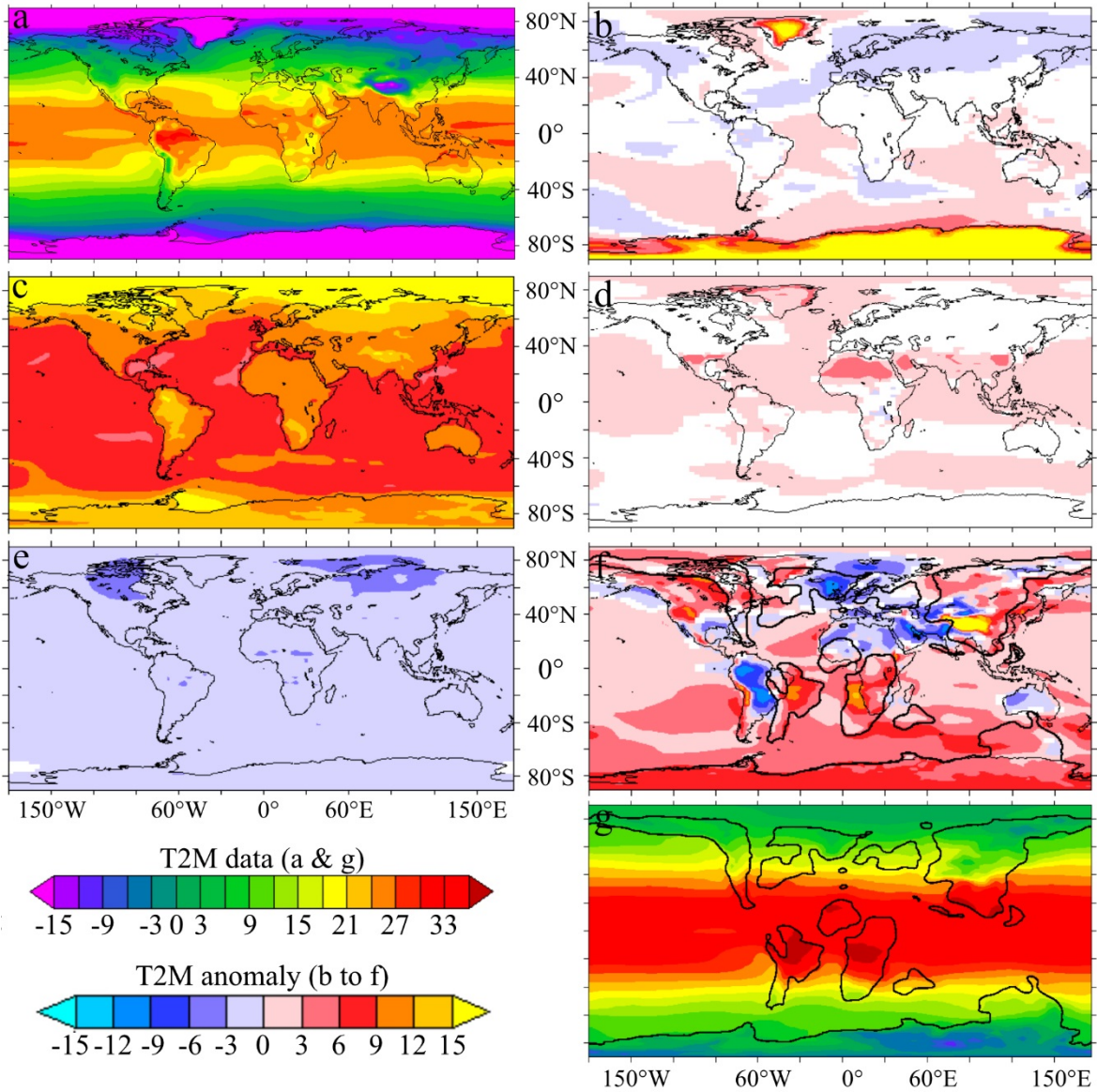
586
587
588
589
590
591
592
593
594
595
596

Figure 5: Mean annual cloudiness for 1X-NOICE and 4X-NOICE simulations. (a) Anomaly of total cloudiness (4X-NOICE – 1X NOICE). (b) Low-altitude cloudiness (Below 680 hPa of atmospheric pressure - solid curves) and high-altitude cloudiness Above 440 hPa of atmospheric pressure - dashed curves) for 1X-NOICE (black) and 4X-NOICE (red) simulations.
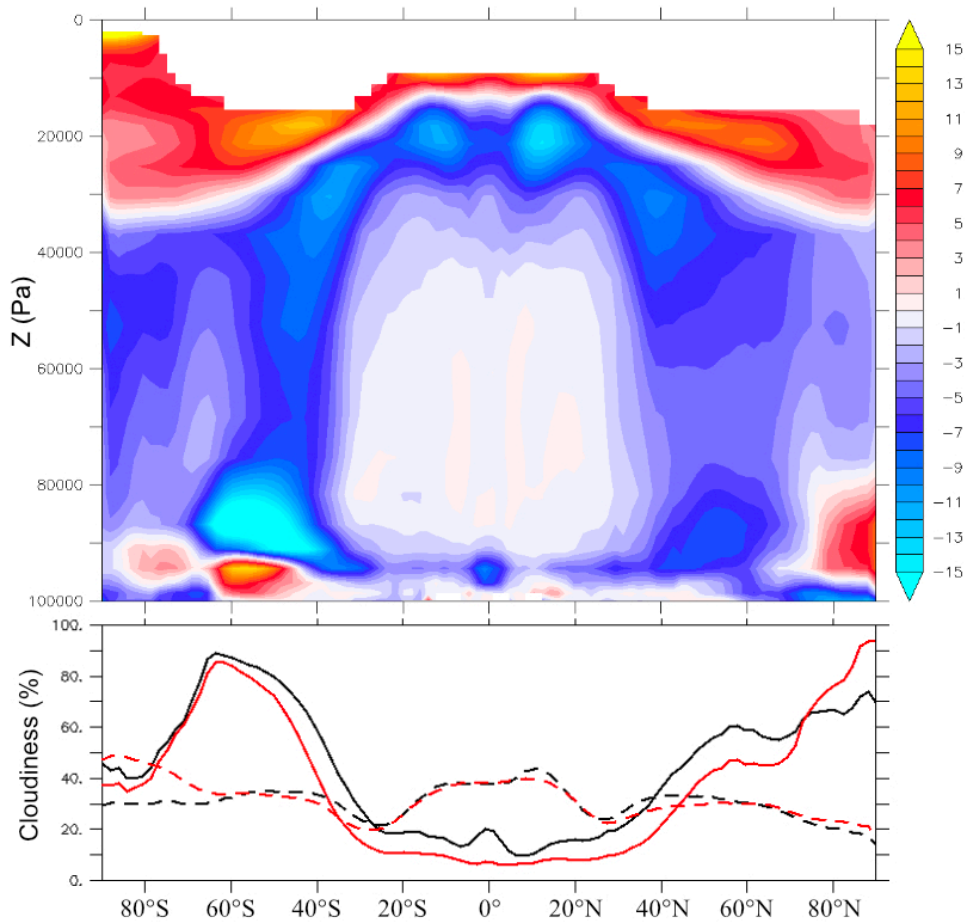
Figure 6: T2M (°C) mean annual meridional gradients for 4X-NI-PFT-SOIL-SOLAR (black) and 4X-CRETACEOUS (red) simulations. Solid curve corresponds to annual average, dashed curves correspond to winter and summer values. The 4X-CRETACEOUS simulation is generally warmer than the 4X-NI-PFT-SOIL-SOLAR-SOLAR simulation, with the exception of the boreal summer.

597
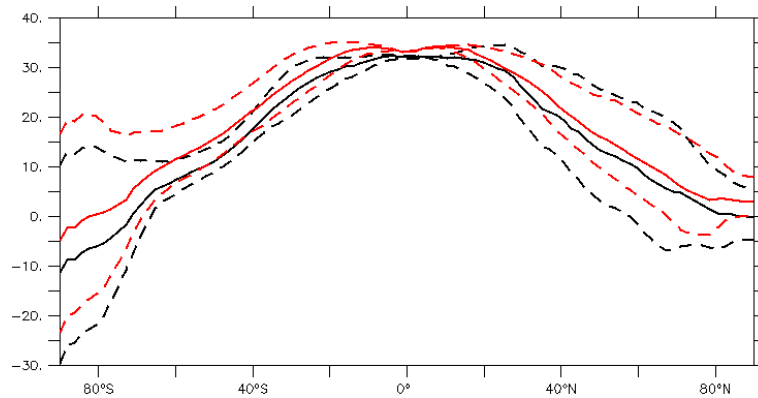
Figure 7: Surface currents for 4X-NOICE-PFT-SOIL-SOLAR (left) and 4X-CRETACEOUS (right) simulations. (a), (b) Intensity of surface circulation (Sv – Annual Mean for 0-80 meters of water depth). Strong equatorial winds lead to the formation of an equatorial circumglobal current. (c), (d) Intensity of surface circulation (Sv – Annual Mean for 0-80 meters of water depth). The closure of the Drake passage (DP-300 meters of water depth) leads to the suppression of the ACC.
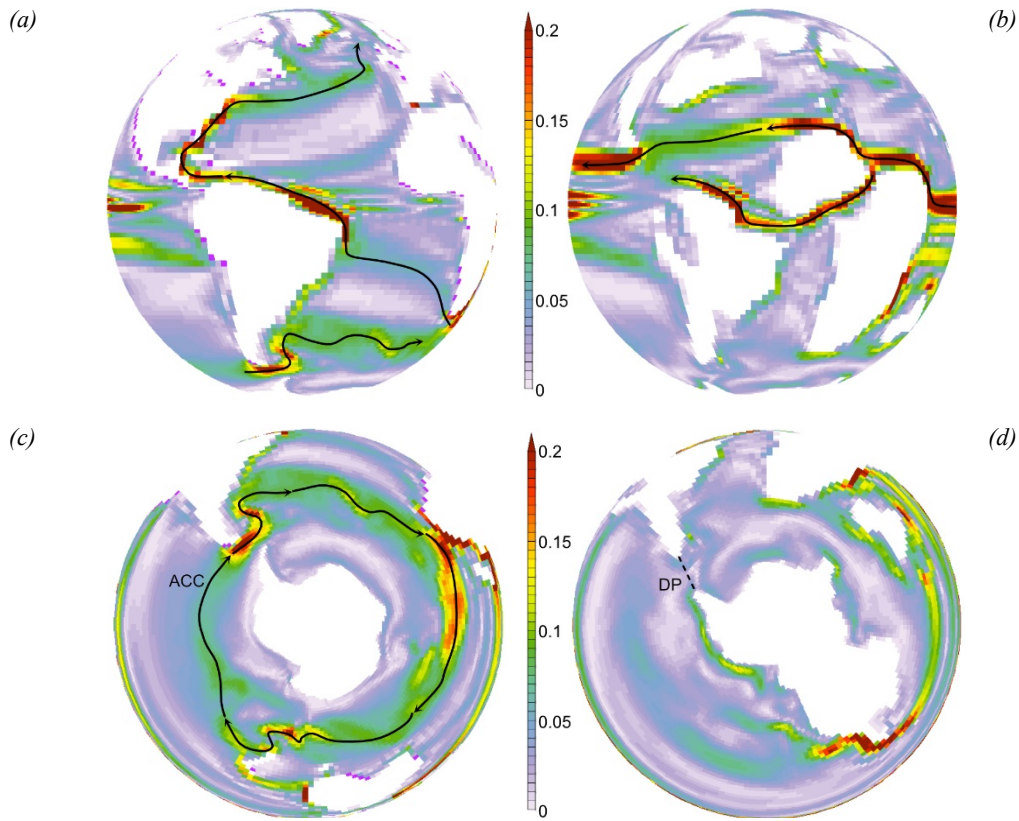
598

599
600

601

602

603

604

605

606
607
608
609

Figure 8 - (a), (b) Global mean annual meridional stream-function (Sv) for the first 300 meters of water depth. Red and blue colors indicate clockwise and anti-clockwise circulation respectively. (a): 4X-NI-PFT-SOIL-SOLAR and (b) 4X-CRETACEOUS. (c) Oceanic heat transport for 4X-NI-PFT-SOIL-SOLAR and 4X-CRETACEOUS simulations. Positive and negative values indicate northward and southward transport direction, respectively.
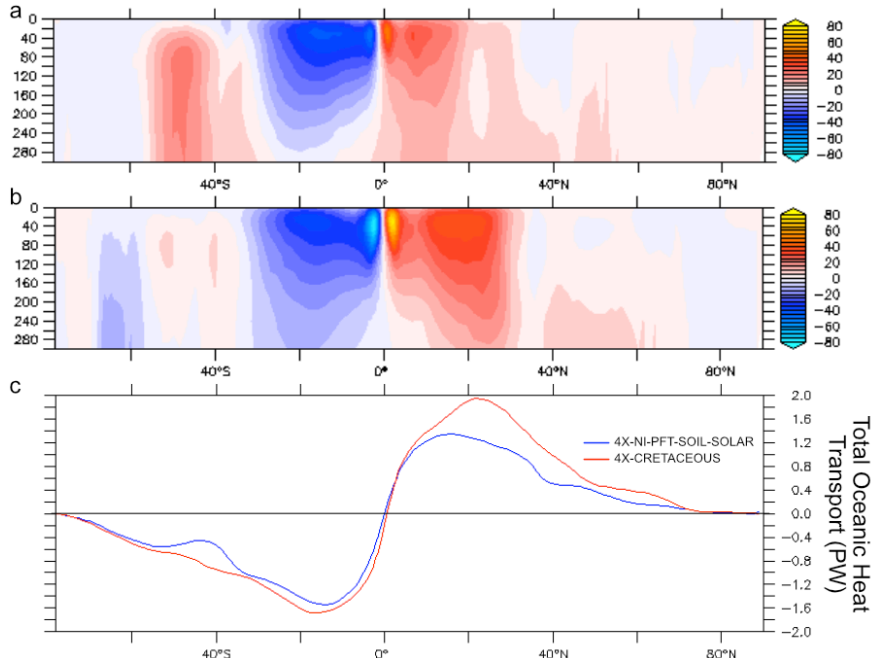
Figure 9: (a) Mean annual meridional Sea-Surface Temperature gradients for all simulations. (b) Same SST curves than (a) but superimposed such as equator temperatures are equal, allowing to compare the steepness of the curves. (c) Meridional atmospheric surface temperature gradients for all simulations. (d) Same curves than (c) but superimposed such as equator temperatures are equal.

(a)   *(b)*

(c)   *(d)*
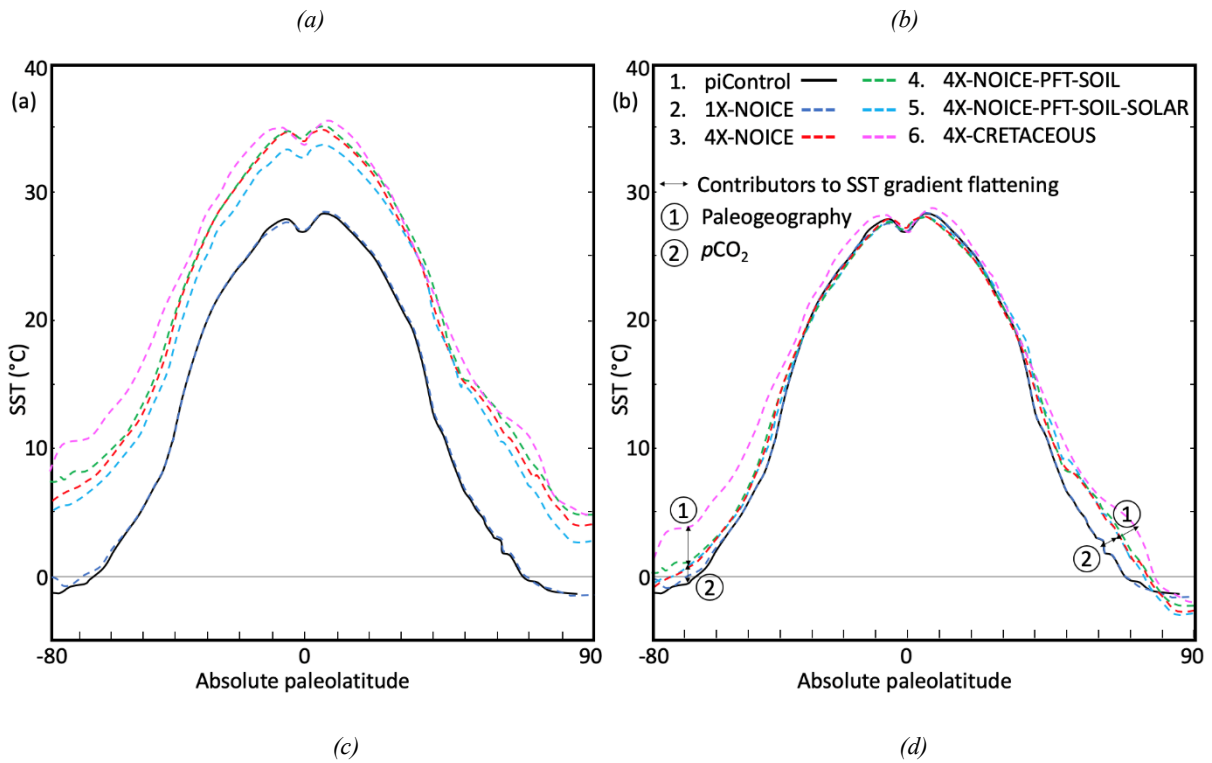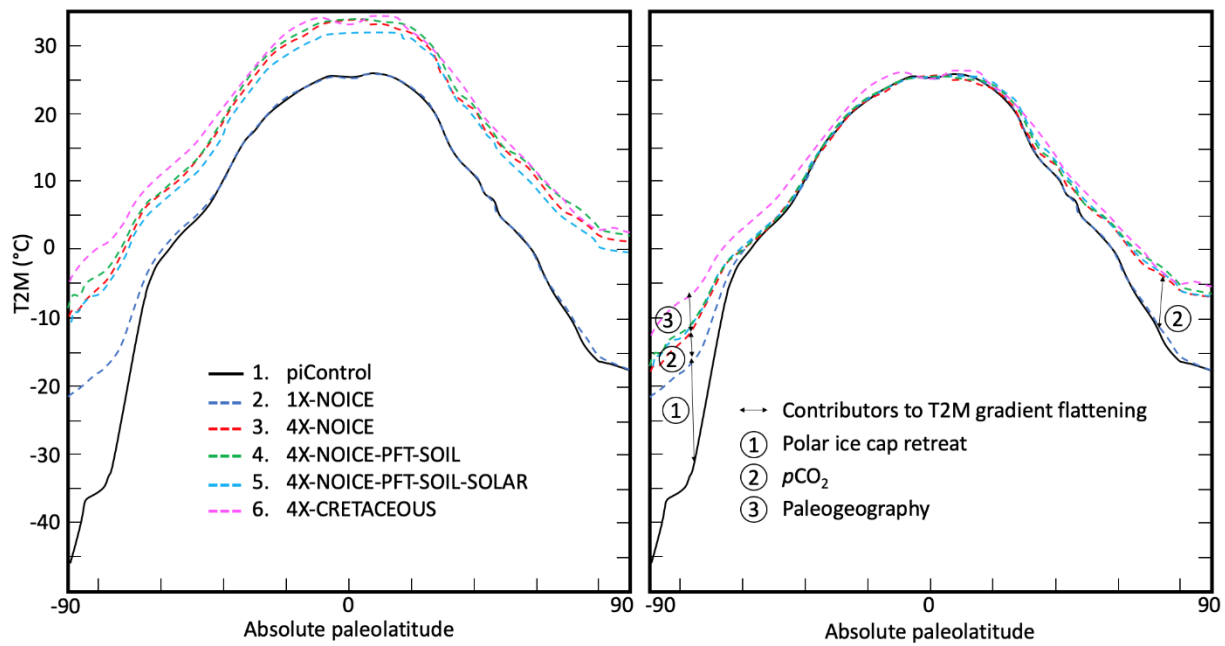
Figure 10: Meridional surface temperature gradients for the 4X-CRETACEOUS simulation. (a) Oceanic temperatures: the solid line corresponds to the mean annual temperature obtained from the modeling. Dashed lines correspond to winter and summer seasonal averages. The grey shaded areas correspond to local monthly temperatures. Data points are obtained with several proxies for the Cenomano-Turonian period. The green data point is obtained from TEX 86 for the Maastrichtian (70 Ma) and extrapolated for 90 Ma. The Huber et al. (2018) point is obtained from $\delta^{18}0$ on foraminifera and the Vandenmark et al., 2007 point is interpreted from the presence of crocodilian fossils. MAT=Mean Annual Temperature, CM=Coldest Month. (b) Atmospheric temperatures: same legend as (a) for modelized temperatures. Data points are obtained from several proxies including CLAMP analysis on paleofloras, leaf analyses, paleosol-derived climofunction or bioclimatic analysis. Symbols represent mean annual temperatures and solid lines associated ranges/errors. Dashed lines represent monthly mean temperatures. Orange data points are for Cenomano-Turonian ages (100-90 Ma), blue data points for Albian and green data points for Coniacian-Santonian (88-85 Ma).
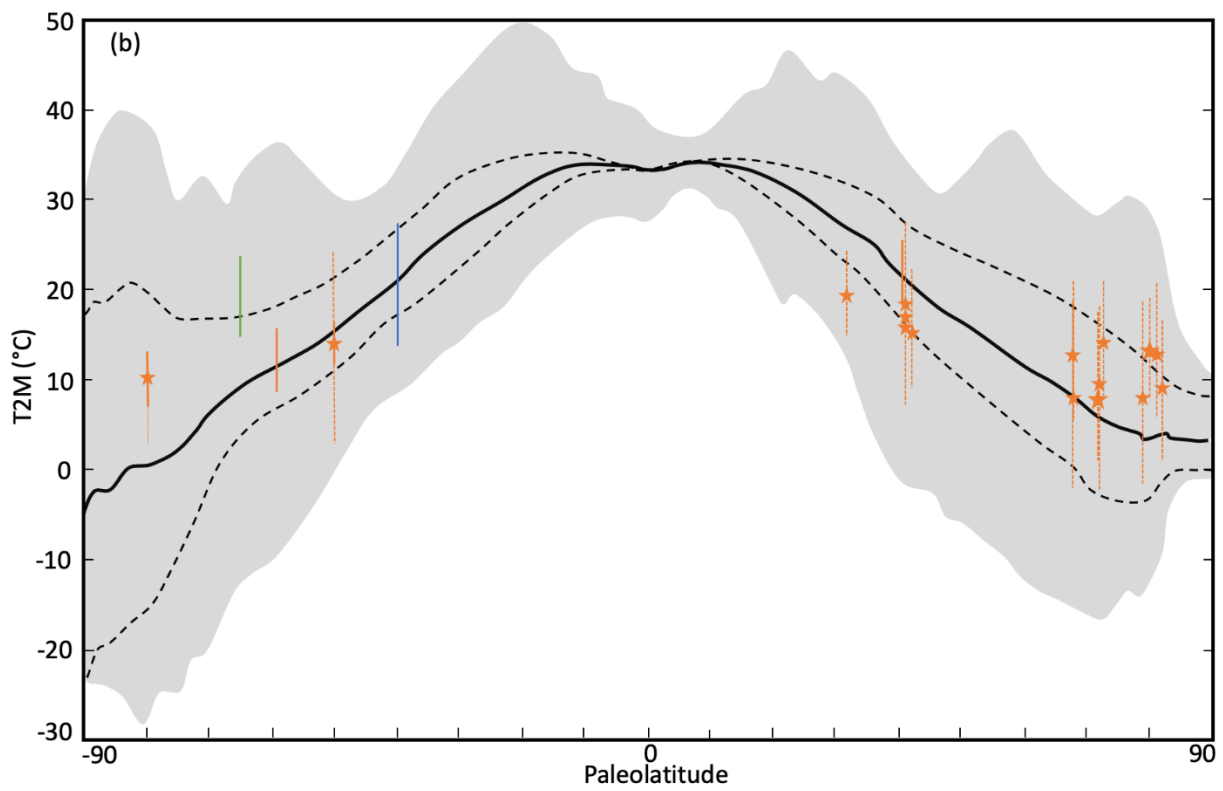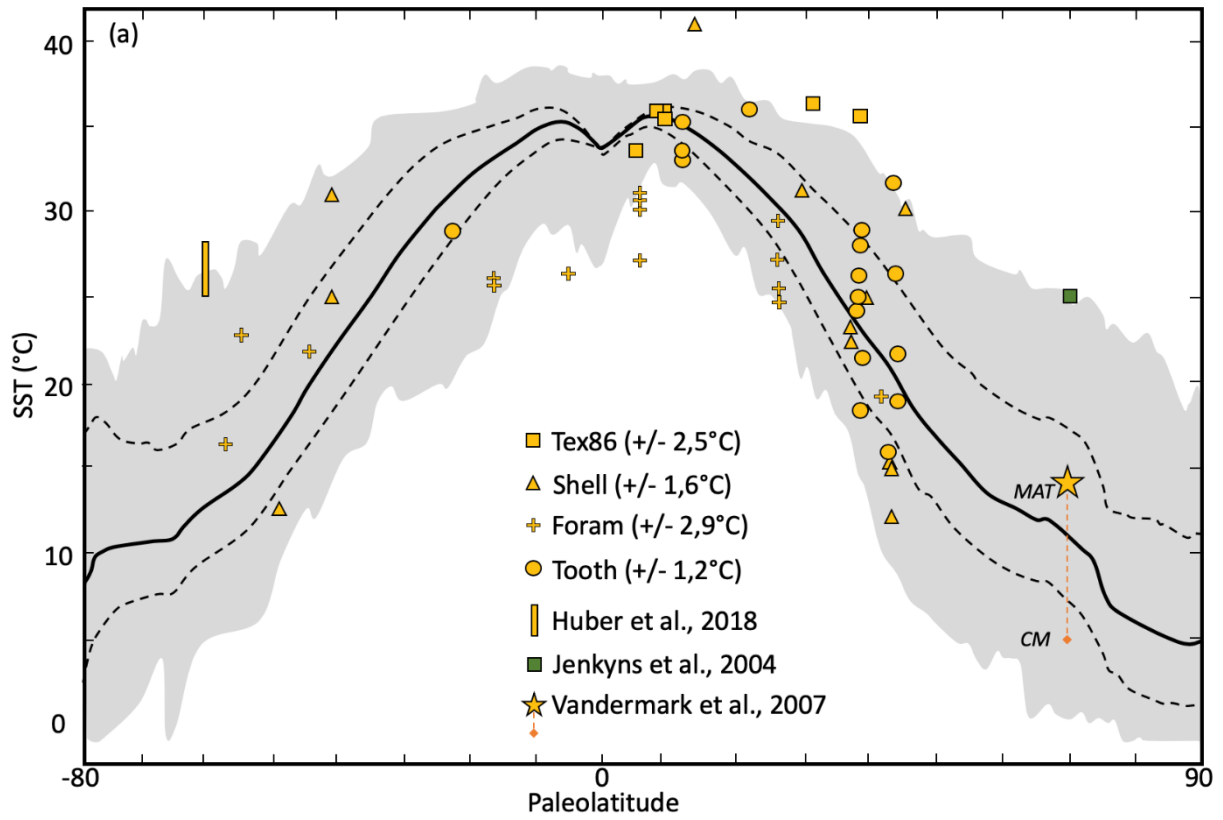
Figure 11: Plot of atmospheric and sea surface mean annual temperature gradients vs pCO₂ for different modelling studies and data compilation. Data gradients are plotted for a default pCO₂ value of 4 P.A.L. Gradients are expressed in °C per °latitude and are calculated from 30 to 80 degrees of latitude. Gradients linked by a line correspond to studies realized with the same model & paleogeography. Solid lines or gradients marked with a (E) correspond to an Eocene paleogeography. Dashed lines or gradients marked with a C correspond to a Cretaceous paleogeography.
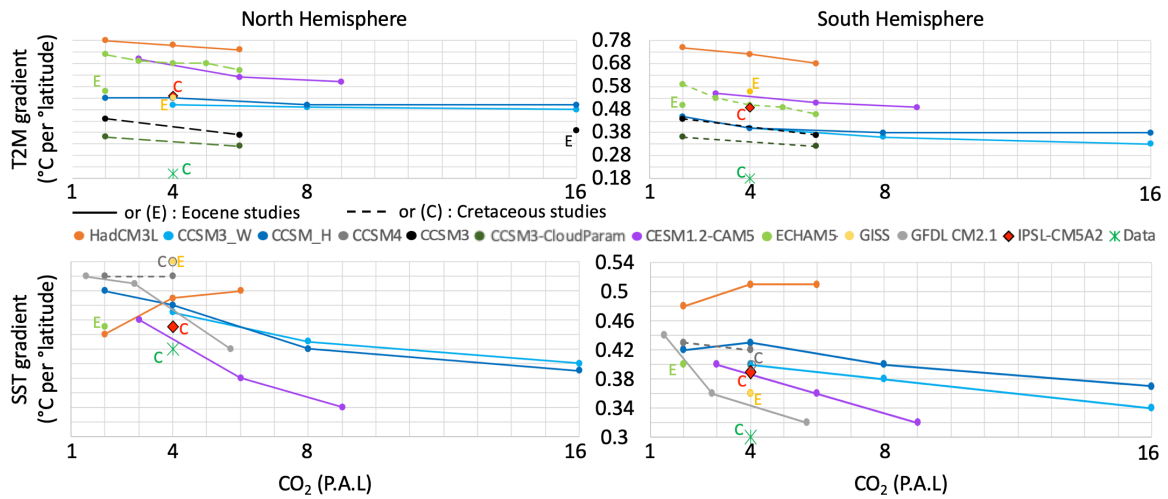
REFERENCES

Aumont, O. and Bopp, L.: Globalizing results from ocean in situ iron fertilization studies, Global Biogeochem. Cycles, 20(2), 1–15, doi:10.1029/2005GB002591, 2006.

Aumont, O., Ethé, C., Tagliabue, A., Bopp, L. and Gehlen, M.: PISCES-v2: An ocean biogeochemical model for carbon and ecosystem studies, Geosci. Model Dev., 8(8), 2465–2513, doi:10.5194/gmd-8-2465-2015, 2015.

Barclay, R. S., McElwain, J. C. and Sageman, B. B.: Carbon sequestration activated by a volcanic CO 2 pulse during Ocean Anoxic Event 2, Nat. Geosci., 3(3), 205–208, doi:10.1038/ngeo757, 2010.

Barron, E. J.: Model simulations of Cretaceous climates : the role of geography and carbon dioxide, , 1(1989), 1993.

Barron, E. J., Fawcett, P. J., Peterson, W. H., Pollard, D. and Thompson, S. L.: A " simulation " of mid-Cretaceous climate Abstract . A series of general circulation model experiments W increased from present day). By combining all three major variables levels of CO2 . Four times present-day • s W provided the best match to the this, , 10(5), 953–962, 1995.

Van Bentum, E. C., Reichart, G. J., Forster, A. and Sinninghe Damsté, J. S.: Latitudinal differences in the amplitude of the OAE-2 carbon isotopic excursion: PCO2and paleo

661   productivity, Biogeosciences, 9(2), 717–731, doi:10.5194/bg-9-717-2012, 2012.

662   Berner, R. A.: GEOCARBSULF: A combined model for Phanerozoic atmospheric O2 and

663   CO2, Geochim. Cosmochim. Acta, 70(23 SPEC. ISS.), 5653–5664,

664   doi:10.1016/j.gca.2005.11.032, 2006.

665   Bice, K. L. and Norris, R. D.: Possible atmospheric CO 2 extremes of the Middle Cretaceous

666   (late Albian-Turonian) , Paleoceanography, 17(4), 22-1-22–17, doi:10.1029/2002pa000778,

667   2003.

668   Bice, K. L., Birgel, D., Meyers, P. A., Dahl, K. A., Hinrichs, K. U. and Norris, R. D.: A

669   multiple proxy and model study of Cretaceous upper ocean temperatures and atmospheric

670   CO2 concentrations, Paleoceanography, 21(2), 1–17, doi:10.1029/2005PA001203, 2006.

671   Bopp, L., Resplandy, L., Orr, J. C., Doney, S. C., Dunne, J. P., Gehlen, M., Halloran, P.,

672   Heinze, C., Ilyina, T., Séférian, R., Tjiputra, J. and Vichi, M.: Multiple stressors of ocean

673   ecosystems in the 21st century: Projections with CMIP5 models, Biogeosciences, 10(10),

674   6225–6245, doi:10.5194/bg-10-6225-2013, 2013.

675   Bopp, L., Resplandy, L., Untersee, A., Le Mezo, P. and Kageyama, M.: Ocean

676   (de)oxygenation from the Last Glacial Maximum to the twenty-first century: Insights from

677   Earth System models, Philos. Trans. R. Soc. A Math. Phys. Eng. Sci., 375(2102),

678   doi:10.1098/rsta.2016.0323, 2017.

679   Brady, E. C., Deconto, R. M. and Thompson, S. L.: Deep Water Formation and Poleward

680   Ocean Heat Transport in the Warm Climate Extreme of the Cretaceous (80 Ma) evidence, ,

681   25(22), 4205–4208, 1998.

682   Broccoli, A. J. and Manabe, S.: The influence of continental ice, atmospheric CO2, and land

683   albedo on the climate of the last glacial maximum, Clim. Dyn., 1(2), 87–99,

684   doi:10.1007/BF01054478, 1987.

685   Bush, A. B. G., George, S. and Philander, H.: The late Cretaceous ' Simulation with a coupled

686   atmosphere-ocean general circulation model, , 12(3), 495–516, 1997.

687   Charney, J., Arakawa, A., Baker, D. ., Bolin, B., Dickinson, R. E., Goody, R. ., Leith, C. .,

688   Stommel, H. . and Wunsch, C. .: Carbon Dioxide and Climate, National Academies Press,

689   Washington, D.C., 1979.

690   Contoux, C., Jost, A., Ramstein, G., Sepulchre, P., Krinner, G. and Schuster, M.: Megalake

691   chad impact on climate and vegetation during the late Pliocene and the mid-Holocene, Clim.

692   Past, 9(4), 1417–1430, doi:10.5194/cp-9-1417-2013, 2013.

693   Contoux, C., Dumas, C., Ramstein, G., Jost, A. and Dolan, A. M.: Modelling Greenland ice

694   sheet inception and sustainability during the Late Pliocene, Earth Planet. Sci. Lett., 424, 295–

695   305, doi:10.1016/j.epsl.2015.05.018, 2015.

696   Crowley, T. J. and Berner, R. A.: CO2 and climate change, Science (80-.)., 292(5518), 870–

697   872, doi:10.1126/science.1061664, 2001.

698   Crowley, T. J. and Zachos, J. C.: Comparison of zonal temperature profiles for past warm

699   time periods, in Warm Climates in Earth History, edited by B. T. Huber, K. G. Macleod, and

700   S. L. Wing, pp. 50–76, Cambridge University Press, Cambridge., 1999.

701   Crowley, T. J., Short, D. A., Mengel, J. G. and North, G. R.: Role of seasonality in the

702   evolution of climate during the last 100 million years, Science (80-.)., 231(4738), 579–584,

703   doi:10.1126/science.231.4738.579, 1986.

704   Damsté, J. S. S., Kuypers, M. M. M., Pancost, R. D. and Schouten, S.: The carbon isotopic

705   response of algae, (cyano)bacteria, archaea and higher plants to the late Cenomanian

706   perturbation of the global carbon cycle: Insights from biomarkers in black shales from the

707   Cape Verde Basin (DSDP Site 367), Org. Geochem., 39(12), 1703–1718,

708   doi:10.1016/j.orggeochem.2008.01.012, 2008.

709   Deconto, R. M., Brady, E. C., Bergengren, J. and Hay, W. W.: Late Cretaceous climate,

710   vegetation, and ocean interactions, Warm Clim. Earth Hist., 275–296,

711   doi:10.1017/cbo9780511564512.010, 2000.

712   Von Deimling, T. S., Ganopolski, A., Held, H. and Rahmstorf, S.: How cold was the last

713   Glacial maximum?, Geophys. Res. Lett., 33(14), 1–5, doi:10.1029/2006GL026484, 2006.

714   Donnadieu, Y., Pierrehumbert, R., Jacob, R. and Fluteau, F.: Modelling the primary control of

715   paleogeography on Cretaceous climate, Earth Planet. Sci. Lett., 248(1–2), 411–422,

716   doi:10.1016/j.epsl.2006.06.007, 2006.

717   Dufresne, J. L., Foujols, M. A., Denvil, S., Caubel, A., Marti, O., Aumont, O., Balkanski, Y.,

718   Bekki, S., Bellenger, H., Benshila, R., Bony, S., Bopp, L., Braconnot, P., Brockmann, P.,

719   Cadule, P., Cheruy, F., Codron, F., Cozic, A., Cugnet, D., de Noblet, N., Duvel, J. P., Ethé,

720   C., Fairhead, L., Fichefet, T., Flavoni, S., Friedlingstein, P., Grandpeix, J. Y., Guez, L.,

721   Guilyardi, E., Hauglustaine, D., Hourdin, F., Idelkadi, A., Ghattas, J., Joussaume, S.,

722   Kageyama, M., Krinner, G., Labetoulle, S., Lahellec, A., Lefebvre, M. P., Lefevre, F., Levy,

723   C., Li, Z. X., Lloyd, J., Lott, F., Madec, G., Mancip, M., Marchand, M., Masson, S.,

724   Meurdesoif, Y., Mignot, J., Musat, I., Parouty, S., Polcher, J., Rio, C., Schulz, M.,

725   Swingedouw, D., Szopa, S., Talandier, C., Terray, P., Viovy, N. and Vuichard, N.: Climate

726   change projections using the IPSL-CM5 Earth System Model: From CMIP3 to CMIP5., 2013.

727   Egbert, G. D., Ray, R. D. and Bills, B. G.: Numerical modeling of the global semidiurnal tide

728   in the present day and in the last glacial maximum, J. Geophys. Res. C Ocean., 109(3), 1–15,

729   doi:10.1029/2003jc001973, 2004.

730   Enderton, D. and Marshall, J.: Explorations of Atmosphere–Ocean–Ice Climates on an

731   Aquaplanet and Their Meridional Energy Transports, J. Atmos. Sci., 66(6), 1593–1611,

732   doi:10.1175/2008jas2680.1, 2008.

733   Fichefet, T. and Maqueda, M. A. M.: Sensitivity of a global sea ice model to the treatment of

734   ice thermodynamics and dynamics, J. Geophys. Res. Ocean., 102(C6), 12609–12646,

735   doi:10.1029/97JC00480, 1997.

736   Fletcher, B. J., Brentnall, S. J., Quick, W. P. and Beerling, D. J.: BRYOCARB: A process-

737   based model of thallose liverwort carbon isotope fractionation in response to CO2, O2, light

738   and temperature, Geochim. Cosmochim. Acta, 70(23 SPEC. ISS.), 5676–5691,

739   doi:10.1016/j.gca.2006.01.031, 2006.

740   Fluteau, F., Ramstein, G., Besse, J., Guiraud, R. and Masse, J. P.: Impacts of palaeogeography

741   and sea level changes on Mid-Cretaceous climate, Palaeogeogr. Palaeoclimatol. Palaeoecol.,

742   247(3–4), 357–381, doi:10.1016/j.palaeo.2006.11.016, 2007.

743   Foster, G. L., Royer, D. L. and Lunt, D. J.: Future climate forcing potentially without

744   precedent in the last 420 million years, Nat. Commun., 8, 1–8, doi:10.1038/ncomms14845,

745   2017.

746   Friedrich, O., Norris, R. D. and Erbacher, J.: Evolution of middle to late Cretaceous oceans-A

747   55 m.y. Record of Earth's temperature and carbon cycle, Geology, 40(2), 107–110,

748   doi:10.1130/G32701.1, 2012.

749   Gastineau, G., D'Andrea, F. and Frankignoul, C.: Atmospheric response to the North Atlantic

750   Ocean variability on seasonal to decadal time scales, Clim. Dyn., 40(9–10), 2311–2330,

751   doi:10.1007/s00382-012-1333-0, 2013.

752   Gates, W. L., Boyle, J. S., Covey, C., Dease, C. G., Doutriaux, C. M., Drach, R. S., Fiorino,

753   M., Gleckler, P. J., Hnilo, J. J., Marlais, S. M., Phillips, T. J., Potter, G. L., Santer, B. D.,

754   Sperber, K. R., Taylor, K. E. and Williams, D. N.: An Overview of the Results of the

755   Atmospheric Model Intercomparison Project (AMIP I), Bull. Am. Meteorol. Soc., 80(1), 29–

756   55 [online] Available from: http://www.jstor.org/stable/26214897, 1999.

757   Goddéris, Y., Donnadieu, Y., Le Hir, G., Lefebvre, V. and Nardin, E.: The role of

758   palaeogeography in the Phanerozoic history of atmospheric CO2and climate, Earth-Science

759   Rev., 128, 122–138, doi:10.1016/j.earscirev.2013.11.004, 2014.

760   Golaz, J., Caldwell, P. M., Van Roekel, L. P., Petersen, M. R., Tang, Q., Wolfe, J. D.,

761   Abeshu, G., Anantharaj, V., Asay-Davis, X. S., Bader, D. C., Baldwin, S. A., Bisht, G.,

762   Bogenschutz, P. A., Branstetter, M., Brunke, M. A., Brus, S. R., Burrows, S. M., Cameron-

Smith, P. J., Donahue, A. S., Deakin, M., Easter, R. C., Evans, K. J., Feng, Y., Flanner, M.,

Foucar, J. G., Fyke, J. G., Griffin, B. M., Hannay, C., Harrop, B. E., Hunke, E. C., Jacob, R.

L., Jacobsen, D. W., Jeffery, N., Jones, P. W., Keen, N. D., Klein, S. A., Larson, V. E.,

Leung, L. R., Li, H., Lin, W., Lipscomb, W. H., Ma, P., Mahajan, S., Maltrud, M. E.,

Mametjanov, A., McClean, J. L., McCoy, R. B., Neale, R. B., Price, S. F., Qian, Y., Rasch, P.

J., Reeves Eyre, J. E. J., Riley, W. J., Ringler, T. D., Roberts, A. F., Roesler, E. L., Salinger,

A. G., Shaheen, Z., Shi, X., Singh, B., Tang, J., Taylor, M. A., Thornton, P. E., Turner, A. K.,

Veneziani, M., Wan, H., Wang, H., Wang, S., Williams, D. N., Wolfram, P. J., Worley, P. H.,

Xie, S., Yang, Y., Yoon, J., Zelinka, M. D., Zender, C. S., Zeng, X., Zhang, C., Zhang, K.,

Zhang, Y., Zheng, X., Zhou, T. and Zhu, Q.: The DOE E3SM coupled model version 1:

Overview and evaluation at standard resolution, J. Adv. Model. Earth Syst., 1–82,

doi:10.1029/2018ms001603, 2019.

Goldner, A., Herold, N. and Huber, M.: Antarctic glaciation caused ocean circulation changes

at the Eocene-Oligocene transition, Nature, 511(7511), 574–577, doi:10.1038/nature13597,

2014.

Gough: Solar interior structure variations*, Sol. Phys., 74(September 1980), 21–34, 1981.

Green, J. A. M. and Huber, M.: Tidal dissipation in the early Eocene and implications for

ocean mixing, Geophys. Res. Lett., 40(11), 2707–2713, doi:10.1002/grl.50510, 2013.

Gyllenhaal, E. D., Engberts, C. J., Markwick, P. J., Smith, L. H. and Patzkowsky, M. E.: The

Fujita-Ziegler model: a new semi-quantitative technique for estimating paleoclimate from

paleogeographic maps, Palaeogeogr. Palaeoclimatol. Palaeoecol., 86(1–2), 41–66,

doi:10.1016/0031-0182(91)90005-C, 1991.

Hay, W. W., DeConto, R. M., de Boer, P., Flögel, S., Song, Y. and Stepashko, A.: Possible

solutions to several enigmas of Cretaceous climate, Springer Berlin Heidelberg., 2019.

Heinemann, M., Jungclaus, J. H. and Marotzke, J.: Warm Paleocene/Eocene climate as

simulated in ECHAM5/MPI-OM, Clim. Past, 5(4), 785–802, doi:10.5194/cp-5-785-2009,

2009.

Herman, A. B. and Spicer, R. A.: Palaeobotanical evidence for a warm Cretaceous Arctic

Ocean, Nature, 380(6572), 330–333, doi:10.1038/380330a0, 1996.

Herman, A. B. and Spicer, R. A.: Mid-Cretaceous floras and climate of the Russian high

Arctic (Novosibirsk Islands, Northern Yakutiya), Palaeogeogr. Palaeoclimatol. Palaeoecol.,

295(3–4), 409–422, doi:10.1016/j.palaeo.2010.02.034, 2010.

Herweijer, C., Seager, R., Winton, M. and Clement, A.: Why ocean heat transport warms the

global mean climate, Tellus, Ser. A Dyn. Meteorol. Oceanogr., 57(4), 662–675,

797 doi:10.1111/j.1600-0870.2005.00121.x, 2005.

798 Hollis, C. J., Taylor, K. W. R., Handley, L., Pancost, R. D., Huber, M., Creech, J. B., Hines,

799 B. R., Crouch, E. M., Morgans, H. E. G., Crampton, J. S., Gibbs, S., Pearson, P. N. and

800 Zachos, J. C.: Early Paleogene temperature history of the Southwest Pacific Ocean :

801 Reconciling proxies and models, Earth Planet. Sci. Lett., 349–350, 53–66,

802 doi:10.1016/j.epsl.2012.06.024, 2012.

803 Hong, S. K. and Lee, Y. Il: Evaluation of atmospheric carbon dioxide concentrations during

804 the Cretaceous, Earth Planet. Sci. Lett., 327–328, 23–28, doi:10.1016/j.epsl.2012.01.014,

805 2012.

806 Hotinski, R. M. and Toggweiler, J. R.: Impact of a Tethyan circumglobal passage on ocean

807 heat transport and "equable" climates, Paleoceanography, 18(1), n/a-n/a,

808 doi:10.1029/2001PA000730, 2003.

809 Hourdin, F., Foujols, M. A., Codron, F., Guemas, V., Dufresne, J. L., Bony, S., Denvil, S.,

810 Guez, L., Lott, F., Ghattas, J., Braconnot, P., Marti, O., Meurdesoif, Y. and Bopp, L.: Impact

811 of the LMDZ atmospheric grid configuration on the climate and sensitivity of the IPSL-

812 CM5A coupled model, Clim. Dyn., 40(9–10), 2167–2192, doi:10.1007/s00382-012-1411-3,

813 2013.

814 Huber, B. T., Hodell, D. A. and Hamilton, C. P.: … Late Cretaceous climate of the southern

815 high latitudes: Stable isotopic evidence for minimal …, Geol. Soc. Am. Bull., (10), 1164–

816 1191, doi:10.1130/0016-7606(1995)107<1164, 1995.

817 Huber, B. T., Leckie, R. M., Norris, R. D., Bralower, T. J. and CoBabe, E.: Foraminiferal

818 assemblage and stable isotopic change across the Cenomanian-Turonian boundary in the

819 Subtropical North Atlantic, J. Foraminifer. Res., 29(4), 392–417, 1999.

820 Huber, B. T., Norris, R. D. and MacLeod, K. G.: Deep-sea paleotemperature record of

821 extreme warmth during the Cretaceous, Geology, 30(2), 123–126, doi:10.1130/0091-

822 7613(2002)030<0123:DSPROE>2.0.CO;2, 2002.

823 Huber, B. T., MacLeod, K. G., Watkins, D. K. and Coffin, M. F.: The rise and fall of the

824 Cretaceous Hot Greenhouse climate, Glob. Planet. Change, 167(April), 1–23,

825 doi:10.1016/j.gloplacha.2018.04.004, 2018.

826 Huber, M.: Progress in Greenhouse Climate Modeling, Paleontol. Soc. Pap., 18, 213–262,

827 doi:10.1017/s108933260000262x, 2012.

828 Huber, M. and Caballero, R.: The early Eocene equable climate problem revisited, Clim. Past,

829 7(2), 603–633, doi:10.5194/cp-7-603-2011, 2011.

830 Hunter, S. J., Haywood, A. M., Valdes, P. J., Francis, J. E. and Pound, M. J.: Modelling

831   equable climates of the Late Cretaceous: Can new boundary conditions resolve data-model

832   discrepancies?, Palaeogeogr. Palaeoclimatol. Palaeoecol., 392, 41–51,

833   doi:10.1016/j.palaeo.2013.08.009, 2013.

834   Hutchinson, D. K., De Boer, A. M., Coxall, H. K., Caballero, R., Nilsson, J. and Baatsen, M.:

835   Climate sensitivity and meridional overturning circulation in the late Eocene using GFDL

836   CM2.1, Clim. Past, 14(6), 789–810, doi:10.5194/cp-14-789-2018, 2018.

837   IPCC: Climate Change 2014: Synthesis Report. Contribution of Working Groups I, II and III

838   to the Fifth Assessment Report of the Intergovernmental Panel on Climate Change., 2014.

839   Jenkyns, H. C.: Geochemistry of oceanic anoxic events, Geochemistry, Geophys.

840   Geosystems, 11(3), 1–30, doi:10.1029/2009GC002788, 2010.

841   Jenkyns, H. C., Forster, A., Schouten, S. and Sinninghe Damsté, J. S.: High temperatures in

842   the Late Cretaceous Arctic Ocean, Nature, 432(7019), 888–892, doi:10.1038/nature03143,

843   2004.

844   Kageyama, M., Braconnot, P., Bopp, L., Caubel, A., Foujols, M. A., Guilyardi, E., Khodri,

845   M., Lloyd, J., Lombard, F., Mariotti, V., Marti, O., Roy, T. and Woillez, M. N.: Mid-

846   Holocene and Last Glacial Maximum climate simulations with the IPSL model-part I:

847   Comparing IPSL_CM5A to IPSL_CM4, Clim. Dyn., 40(9–10), 2447–2468,

848   doi:10.1007/s00382-012-1488-8, 2013.

849   Kennedy, A. T., Farnsworth, A., Lunt, D. J., Lear, C. H. and Markwick, P. J.: Atmospheric

850   and oceanic impacts of Antarctic glaciation across the Eocene-Oligocene transition, Philos.

851   Trans. R. Soc. A Math. Phys. Eng. Sci., 373(2054), doi:10.1098/rsta.2014.0419, 2015.

852   Kerr, A. C. and Kerr, A. C.: Oceanic plateau formation : A cause of mass extinction and black

853   shale deposition around the Cenomanian-Turonian boundary ? Oceanic plateau formation : a

854   cause of mass extinction and black shale deposition around the Cenomanian – Turonian

855   boundary ?, , (May), doi:10.1144/gsjgs.155.4.0619, 1998.

856   Knorr, G. and Lohmann, G.: Climate warming during antarctic ice sheet expansion at the

857   middle miocene transition, Nat. Geosci., 7(5), 376–381, doi:10.1038/ngeo2119, 2014.

858   Koch-Larrouy, A., Madec, G., Bouruet-Aubertot, P., Gerkema, T., Bessières, L. and Molcard,

859   R.: On the transformation of Pacific Water into Indonesian Throughflow Water by internal

860   tidal mixing, Geophys. Res. Lett., 34(4), 1–6, doi:10.1029/2006GL028405, 2007.

861   Krinner, G., Viovy, N., de Noblet-Ducoudré, N., Ogée, J., Polcher, J., Friedlingstein, P.,

862   Ciais, P., Sitch, S. and Prentice, I. C.: A dynamic global vegetation model for studies of the

863   coupled atmosphere-biosphere system, Global Biogeochem. Cycles, 19(1), 1–33,

864   doi:10.1029/2003GB002199, 2005.

865   Ladant, J. B. and Donnadieu, Y.: Palaeogeographic regulation of glacial events during the

866   Cretaceous supergreenhouse, Nat. Commun., 7(April 2017), 1–9, doi:10.1038/ncomms12771,

867   2016.

868   Ladant, J. B., Donnadieu, Y., Bopp, L., Lear, C. H. and Wilson, P. A.: Meridional Contrasts

869   in Productivity Changes Driven by the Opening of Drake Passage, Paleoceanogr.

870   Paleoclimatology, 302–317, doi:10.1002/2017PA003211, 2018.

871   de Lavergne, C., Falahat, S., Madec, G., Roquet, F., Nycander, J. and Vic, C.: Toward global

872   maps of internal tide energy sinks, Ocean Model., 137(April), 52–75,

873   doi:10.1016/j.ocemod.2019.03.010, 2019.

874   Leier, A., Quade, J., DeCelles, P. and Kapp, P.: Stable isotopic results from paleosol

875   carbonate in South Asia: Paleoenvironmental reconstructions and selective alteration, Earth

876   Planet. Sci. Lett., 279(3–4), 242–254, doi:10.1016/j.epsl.2008.12.044, 2009.

877   Levine, X. J. and Schneider, T.: Response of the Hadley Circulation to Climate Change in an

878   Aquaplanet GCM Coupled to a Simple Representation of Ocean Heat Transport, J. Atmos.

879   Sci., 68(4), 769–783, doi:10.1175/2010jas3553.1, 2010.

880   Littler, K., Robinson, S. A., Bown, P. R., Nederbragt, A. J. and Pancost, R. D.: High sea-

881   surface temperatures during the Early Cretaceous Epoch, Nat. Geosci., 4(3), 169–172,

882   doi:10.1038/ngeo1081, 2011.

883   Lunt, D. J., Jones, T. D., Heinemann, M., Huber, M., LeGrande, A., Winguth, A., Loptson,

884   C., Marotzke, J., Roberts, C. D., Tindall, J., Valdes, P. and Winguth, C.: A model-data

885   comparison for a multi-model ensemble of early Eocene atmosphere-ocean simulations:

886   EoMIP, Clim. Past, 8(5), 1717–1736, doi:10.5194/cp-8-1717-2012, 2012a.

887   Lunt, D. J., Haywood, A. M., Schmidt, G. A., Salzmann, U., Valdes, P. J., Dowsett, H. J. and

888   Loptson, C. A.: On the causes of mid-Pliocene warmth and polar amplification, Earth Planet.

889   Sci. Lett., 321–322, 128–138, doi:10.1016/j.epsl.2011.12.042, 2012b.

890   Lunt, D. J., Farnsworth, A., Loptson, C., L Foster, G., Markwick, P., O'Brien, C. L., Pancost,

891   R. D., Robinson, S. A. and Wrobel, N.: Palaeogeographic controls on climate and proxy

892   interpretation, Clim. Past, 12(5), 1181–1198, doi:10.5194/cp-12-1181-2016, 2016.

893   Lunt, D. J., Huber, M., Anagnostou, E., Baatsen, M. L. J., Caballero, R., DeConto, R.,

894   Dijkstra, H. A., Donnadieu, Y., Evans, D., Feng, R., Foster, G. L., Gasson, E., Von Der

895   Heydt, A. S., Hollis, C. J., Inglis, G. N., Jones, S. M., Kiehl, J., Turner, S. K., Korty, R. L.,

896   Kozdon, R., Krishnan, S., Ladant, J. B., Langebroek, P., Lear, C. H., LeGrande, A. N., Littler,

897   K., Markwick, P., Otto-Bliesner, B., Pearson, P., Poulsen, C. J., Salzmann, U., Shields, C.,

898   Snell, K., Stärz, M., Super, J., Tabor, C., Tierney, J. E., Tourte, G. J. L., Tripati, A.,

899   Upchurch, G. R., Wade, B. S., Wing, S. L., Winguth, A. M. E., Wright, N. M., Zachos, J. C.

900   and Zeebe, R. E.: The DeepMIP contribution to PMIP4: Experimental design for model

901   simulations of the EECO, PETM, and pre-PETM (version 1.0), Geosci. Model Dev., 10(2),

902   889–901, doi:10.5194/gmd-10-889-2017, 2017.

903   MacLeod, K. G., Huber, B. T., Berrocoso, Á. J. and Wendler, I.: A stable and hot Turonian

904   without glacial δ18O excursions is indicated by exquisitely preserved Tanzanian foraminifera,

905   Geology, 41(10), 1083–1086, doi:10.1130/G34510.1, 2013.

906   Madec, G.: NEMO ocean engine (2012), , (27), 2012.

907   Madec, G. and Imbard, M.: A global ocean mesh to overcome the North Pole singularity,

908   Clim. Dyn., 12(6), 381–388, doi:10.1007/BF00211684, 1996.

909   Maffre, P., Ladant, J. B., Donnadieu, Y., Sepulchre, P. and Goddéris, Y.: The influence of

910   orography on modern ocean circulation, Clim. Dyn., 50(3–4), 1277–1289,

911   doi:10.1007/s00382-017-3683-0, 2018.

912   Mays, C., Steinthorsdottir, M. and Stilwell, J. D.: Climatic implications of Ginkgoites

913   waarrensis Douglas emend. from the south polar Tupuangi flora, Late Cretaceous

914   (Cenomanian), Chatham Islands, Palaeogeogr. Palaeoclimatol. Palaeoecol., 438, 308–326,

915   doi:10.1016/j.palaeo.2015.08.011, 2015.

916   Le Mézo, P., Beaufort, L., Bopp, L., Braconnot, P. and Kageyama, M.: From monsoon to

917   marine productivity in the Arabian Sea: Insights from glacial and interglacial climates, Clim.

918   Past, 13(7), 759–778, doi:10.5194/cp-13-759-2017, 2017.

919   Monteiro, F. M., Pancost, R. D., Ridgwell, A. and Donnadieu, Y.: Nutrients as the dominant

920   control on the spread of anoxia and euxinia across the Cenomanian-Turonian oceanic anoxic

921   event (OAE2): Model-data comparison, Paleoceanography, 27(4), 1–17,

922   doi:10.1029/2012PA002351, 2012.

923   Müller, R. D., Sdrolias, M., Gaina, C. and Roest, W. R.: Age, spreading rates, and spreading

924   asymmetry of the world's ocean crust, Geochemistry, Geophys. Geosystems, 9(4), 1–19,

925   doi:10.1029/2007GC001743, 2008.

926   Niezgodzki, I., Knorr, G., Lohmann, G., Tyszka, J. and Markwick, P. J.: Late Cretaceous

927   climate simulations with different CO2 levels and subarctic gateway configurations: A model-

928   data comparison, Paleoceanography, 32(9), 980–998, doi:10.1002/2016PA003055, 2017.

929   Norris, R. D., Bice, K. L., Magno, E. A. and Wilson, P. A.: Jiggling the tropical thermostat in

930   the Cretaceous hothouse, Geology, 30(4), 299–302, doi:10.1130/0091-

931   7613(2002)030<0299:JTTTIT>2.0.CO;2, 2002.

932   O'Brien, C. L., Robinson, S. A., Pancost, R. D., Sinninghe Damsté, J. S., Schouten, S., Lunt,

933   D. J., Alsenz, H., Bornemann, A., Bottini, C., Brassell, S. C., Farnsworth, A., Forster, A.,

934   Huber, B. T., Inglis, G. N., Jenkyns, H. C., Linnert, C., Littler, K., Markwick, P., McAnena,

935   A., Mutterlose, J., Naafs, B. D. A., Püttmann, W., Sluijs, A., van Helmond, N. A. G. M.,

936   Vellekoop, J., Wagner, T. and Wrobel, N. E.: Cretaceous sea-surface temperature evolution:

937   Constraints from TEX 86 and planktonic foraminiferal oxygen isotopes, Earth-Science Rev.,

938   172(March 2016), 224–247, doi:10.1016/j.earscirev.2017.07.012, 2017.

939   Ohba, M. and Ueda, H.: A GCM Study on Effects of Continental Drift on Tropical Climate at

940   the Early and Late Cretaceous, J. Meteorol. Soc. Japan, 88(6), 869–881,

941   doi:10.2151/jmsj.2010-601, 2011.

942   Ortega, P., Mignot, J., Swingedouw, D., Sévellec, F. and Guilyardi, E.: Reconciling two

943   alternative mechanisms behind bi-decadal variability in the North Atlantic, Prog. Oceanogr.,

944   137, 237–249, doi:10.1016/j.pocean.2015.06.009, 2015.

945   Otto-bliesner, B. L. and Upchurch, G. R.: the Late Cretaceous period, , 385127(February),

946   18–21, 1997.

947   Pearson, P. N., DitchfieldPeter, W., SinganoJoyce, Harcourt-BrownKatherine, G.,

948   NicholasChristopher, J., OlssonRichard, K., ShackletonNicholas, J. and HallMike, A.:

949   erratum: Warm tropical sea surface temperatures in the Late Cretaceous and Eocene epochs,

950   Nature, 414(6862), 470 [online] Available from: http://dx.doi.org/10.1038/35106617, 2001.

951   Poulsen, C. J., Seidov, D., Barron, E. J. and Peterson, W. H.: The impact of paleogeographic

952   evolution on the surface oceanic circulation and the marine environment within the Mid-

953   Cretaceous tethys, , 13(5), 546–559, 1998.

954   Poulsen, C. J., Barron, E. J., Arthur, M. A. and Peterson, W. H.: Response of the mid-

955   Cretaceous global oceanic circulation to tectonic and CO_2 forcings,

956   Paleoceanography, 16(6), 576–592, doi:10.1029/2000PA000579, 2001.

957   Poulsen, C. J., Gendaszek, A. S. and Jacob, R. L.: Did the rifting of the Atlantic Ocean cause

958   the Cretaceous thermal maximum?, Geology, 31(2), 115–118, doi:10.1130/0091-

959   7613(2003)031<0115:DTROTA>2.0.CO;2, 2003.

960   Poulsen, C. J., Pollard, D. and White, T. S.: General circulation model simulation of the δ18O

961   content of continental precipitation in the middle Cretaceous: A model-proxy comparison,

962   Geology, 35(3), 199–202, doi:10.1130/G23343A.1, 2007.

963   Pucéat, E., Lécuyer, C., Donnadieu, Y., Naveau, P., Cappetta, H., Ramstein, G., Huber, B. T.

964   and Kriwet, J.: Fish tooth δ18O revising Late Cretaceous meridional upper ocean water

965   temperature gradients, Geology, 35(2), 107–110, doi:10.1130/G23103A.1, 2007.

966   Retallack, G. J. and Conde, G. D.: Deep time perspective on rising atmospheric CO2, Glob.

967   Planet. Change, 189(March), 103177, doi:10.1016/j.gloplacha.2020.103177, 2020.

968   Robinson, S. A., Dickson, A. J., Pain, A., Jenkyns, H. C., O'Brien, C. L., Farnsworth, A. and

969   Lunt, D. J.: Southern Hemisphere sea-surface temperatures during the Cenomanian-Turonian:

970   Implications for the termination of Oceanic Anoxic Event 2, Geology, 47(2), 131–134,

971   doi:10.1130/G45842.1, 2019.

972   Rose, B. E. J. and Ferreira, D.: Ocean heat transport and water vapor greenhouse in a warm

973   equable climate: A new look at the low gradient paradox, J. Clim., 26(6), 2117–2136,

974   doi:10.1175/JCLI-D-11-00547.1, 2013.

975   Royer, D. L.: Atmospheric CO2 and O2 During the Phanerozoic: Tools, Patterns, and

976   Impacts, 2nd ed., Elsevier Ltd., 2013.

977   Royer, D. L., Berner, R. A. and Park, J.: Climate sensitivity constrained by CO2

978   concentrations over the past 420 million years, Nature, 446(7135), 530–532,

979   doi:10.1038/nature05699, 2007.

980   Sandler, A. and Harlavan, Y.: Early diagenetic illitization of illite-smectite in Cretaceous

981   sediments (Israel): evidence from K-Ar dating, Clay Miner., 41(2), 637–658,

982   doi:10.1180/0009855064120210, 2006.

983   Sarr, A. C., Sepulchre, P. and Husson, L.: Impact of the Sunda Shelf on the Climate of the

984   Maritime Continent, J. Geophys. Res. Atmos., doi:10.1029/2018JD029971, 2019.

985   Schmidt, G. A. and Mysak, L. A.: Can increased poleward oceanic heat flux explain the warm

986   Cretaceous climate?, Paleoceanography, 11(5), 579–593, doi:10.1029/96PA01851, 1996.

987   Sellers, P. ., Bounoua, L., Collatz, G. J., Randall, D. A., Dazlich, D. A., Los, S. O., Berry, J.

988   A., Fung, I., Tucker, C. J., Field, C. B. and Jensen, T. G.: Comparison of Radiative and

989   Physiological Effects of Doubled Atmospheric CO2 on Climate, , 1402–1406, 1996.

990   Sellwood, B. W., Price, G. D. and Valdest, P. J.: Cretaceous temperatures, , 370(August),

991   453–455, 1994.

992   Sepulchre, P., Caubel, A., Ladant, J., Bopp, L., Boucher, O., Braconnot, P., Brockmann, P.,

993   Cozic, A., Donnadieu, Y., Estella-perez, V., Ethé, C., Fluteau, F., Foujols, M., Gastineau, G.,

994   Ghattas, J., Hauglustaine, D., Hourdin, F., Kageyama, M., Khodri, M., Marti, O., Meurdesoif,

995   Y., Mignot, J., Sarr, A., Servonnat, J., Swingedouw, D., Szopa, S. and Tardif, D.: IPSL-

996   CM5A2 . An Earth System Model designed for multi-millennial climate simulations, ,

997   (December), 2019.

998   Sewall, J. O., Van De Wal, R. S. W., Van Der Zwan, K., Van Oosterhout, C., Dijkstra, H. A.

999   and Scotese, C. R.: Climate model boundary conditions for four Cretaceous time slices, Clim.

1000   Past, 3(4), 647–657, doi:10.5194/cp-3-647-2007, 2007.

Simmons, H. L., Jayne, S. R., St. Laurent, L. C. and Weaver, A. J.: Tidally driven mixing in a numerical model of the ocean general circulation, Ocean Model., 6(3–4), 245–263, doi:10.1016/S1463-5003(03)00011-8, 2004.

Sluijs, A., Schouten, S., Pagani, M., Woltering, M. and Brinkhuis, H.: Subtropical Arctic Ocean temperatures during the Palaeocene / Eocene thermal maximum, , (May 2014), doi:10.1038/nature04668, 2006.

Spicer, R. A. and Herman, A. B.: The Late Cretaceous environment of the Arctic: A quantitative reassessment based on plant fossils, Palaeogeogr. Palaeoclimatol. Palaeoecol., 295(3–4), 423–442, doi:10.1016/j.palaeo.2010.02.025, 2010.

Steinig, S., Dummann, W., Park, W., Latif, M., Kusch, S., Hofmann, P. and Flögel, S.: Evidence for a regional warm bias in the Early Cretaceous TEX86 record, Earth Planet. Sci. Lett., 539, 116184, doi:10.1016/j.epsl.2020.116184, 2020.

Swingedouw, D., Rodehacke, C. B., Olsen, S. M., Menary, M., Gao, Y., Mikolajewicz, U. and Mignot, J.: On the reduced sensitivity of the Atlantic overturning to Greenland ice sheet melting in projections: a multi-model assessment, Clim. Dyn., 44(11–12), 3261–3279, doi:10.1007/s00382-014-2270-x, 2015.

Swingedouw, D., Mignot, J., Guilyardi, E., Nguyen, S. and Ormières, L.: Tentative reconstruction of the 1998–2012 hiatus in global temperature warming using the IPSL–CM5A–LR climate model, Comptes Rendus - Geosci., 349(8), 369–379, doi:10.1016/j.crte.2017.09.014, 2017.

Tabor, C. R., Poulsen, C. J., Lunt, D. J., Rosenbloom, N. A., Otto-Bliesner, B. L., Markwick, P. J., Brady, E. C., Farnsworth, A. and Feng, R.: The cause of Late Cretaceous cooling: A multimodel-proxy comparison, Geology, 44(11), 963–966, doi:10.1130/G38363.1, 2016.

Tagliabue, A., Bopp, L., Dutay, J. C., Bowie, A. R., Chever, F., Jean-Baptiste, P., Bucciarelli, E., Lannuzel, D., Remenyi, T., Sarthou, G., Aumont, O., Gehlen, M. and Jeandel, C.: Hydrothermal contribution to the oceanic dissolved iron inventory, Nat. Geosci., 3(4), 252–256, doi:10.1038/ngeo818, 2010.

Tan, N., Ramstein, G., Dumas, C., Contoux, C., Ladant, J. B., Sepulchre, P., Zhang, Z. and De Schepper, S.: Exploring the MIS M2 glaciation occurring during a warm and high atmospheric CO2Pliocene background climate, Earth Planet. Sci. Lett., 472, 266–276, doi:10.1016/j.epsl.2017.04.050, 2017.

Tierney, J. E.: GDGT Thermometry: Lipid Tools for Reconstructing Paleotemperatures, Paleontol. Soc. Pap., 18, 115–132, doi:10.1017/s1089332600002588, 2012.

Turgeon, S. C. and Creaser, R. A.: Cretaceous oceanic anoxic event 2 triggered by a massive

1035 magmatic episode, , 454(July), doi:10.1038/nature07076, 2008.

1036 Upchurch, G. R.: Vegetation-atmosphere interactions and their role in global warming during

1037 the latest Cretaceous, Philos. Trans. R. Soc. B Biol. Sci., 353(1365), 97–112,

1038 doi:10.1098/rstb.1998.0194, 1998.

1039 Upchurch, G. R., Kiehl, J., Shields, C., Scherer, J. and Scotese, C.: Latitudinal temperature

1040 gradients and high-latitude temperatures during the latest Cretaceous: Congruence of geologic

1041 data and climate models, Geology, 43(8), 683–686, doi:10.1130/G36802.1, 2015.

1042 Valcke, S., Budich, R., Carter, M., Guilyardi, E., Lautenschlager, M., Redler, R. and

1043 Steenman-clark, L.: The PRISM software framework and the OASIS coupler, , 5(September

1044 2014), 2001–2004, 2006.

1045 Vandermark, D., Tarduno, J. A. and Brinkman, D. B.: A fossil champsosaur population from

1046 the high Arctic: Implications for Late Cretaceous paleotemperatures, Palaeogeogr.

1047 Palaeoclimatol. Palaeoecol., 248(1–2), 49–59, doi:10.1016/j.palaeo.2006.11.008, 2007.

1048 Veizer, J., Godderis, Y. and François, L. M.: Evidence for decoupling of atmospheric CO_2

1049 and global climate during the Phanerozoic eon, Nature, 408(6813), 698–701,

1050 doi:10.1038/35047044, 2000.

1051 Wang, Y., Huang, C., Sun, B., Quan, C., Wu, J. and Lin, Z.: Paleo-CO2 variation trends and

1052 the Cretaceous greenhouse climate, Earth-Science Rev., 129, 136–147,

1053 doi:10.1016/j.earscirev.2013.11.001, 2014.

1054 Wilson, M. F. and Henderson-sellers, A.: LBA Regional Vegetation and Soils, 1-Degree

1055 (Wilson and Henderson-Sellers), , doi:10.3334/ORNLDAAC/687, 2003.

1056 Woillez, M. N., Levavasseur, G., Daniau, A. L., Kageyama, M., Urrego, D. H., Sánchez-

1057 Goñi, M. F. and Hanquiez, V.: Impact of precession on the climate, vegetation and fire

1058 activity in southern Africa during MIS4, Clim. Past, 10(3), 1165–1182, doi:10.5194/cp-10-

1059 1165-2014, 2014.

1060 Zhou, J., Poulsen, C. J., Pollard, D. and White, T. S.: Simulation of modern and middle

1061 Cretaceous marine δ18O with an ocean-atmosphere general circulation model,

1062 Paleoceanography, 23(3), 1–11, doi:10.1029/2008PA001596, 2008.

1063 Zhou, J., Poulsen, C. J., Rosenbloom, N., Shields, C. and Briegleb, B.: Vegetation-climate

1064 interactions in the warm mid-Cretaceous, Clim. Past, 8(2), 565–576, doi:10.5194/cp-8-565-

1065 2012, 2012.

1066 Zhu, J., Poulsen, C. J. and Tierney, J. E.: Simulation of Eocene extreme warmth and high

1067 climate sensitivity through cloud feedbacks, Sci. Adv., 5(9), eaax1874,

1068 doi:10.1126/sciadv.aax1874, 2019.

1069   Zhu, J., Poulsen, C. J., Otto-Bliesner, B. L., Liu, Z., Brady, E. C. and Noone, D. C.:

1070   Simulation of early Eocene water isotopes using an Earth system model and its implication

1071   for past climate reconstruction, Earth Planet. Sci. Lett., 537, 116164,

1072   doi:10.1016/j.epsl.2020.116164, 2020.

1073   Zobler, L.: Global Soil Types, 1-Degree Grid (Zobler), , doi:10.3334/ORNLDAAC/418,

1074   1999.

1075

1076

1077